



Cite this: *RSC Adv.*, 2025, 15, 28021

# Plasmonic chemosensing of W(VI), Pd(II), Cr(III), and Cs(I) in deep eutectic solvent using silver nanoparticles: green solvent toward optical point-of-use quality testing

Raana Tayefeh-Rahimian,<sup>ab</sup> Masoud Rismanchian<sup>\*a</sup>  
and Mohammad Hasanzadeh <sup>\*b</sup>

The rapid and accurate detection of heavy metals is essential for reducing environmental pollution. Consequently, the quick and precise identification of heavy metals has become a primary challenge for scientists worldwide. In this study, an innovative and efficient optical chemosensor was developed based on a deep eutectic solvent (DES) for the selective identification of W(VI), Pd(II), Cr(III), and Cs(I) among 30 types of metal ions. A unique optical probe was fabricated by dissolving silver nanoparticles (T-AgNPs) in a DES prepared from ChCl and EG. The color change of the T-AgNPs-DES probe was observed with a smartphone, and a UV-vis spectrometer was used to validate it. The shift in the LSPR band in the UV-vis portion of the spectrum was used for plasmon optical sensing of candidate ions in samples. The proposed optical sensor demonstrated a high degree of linearity in the 0.01 to 0.8  $\mu\text{g mL}^{-1}$  concentration range for W(VI), Pd(II), Cr(III), and Cs(I), respectively. The suggested method for using the T-AgNPs-DES probe to detect W(VI), Pd(II), Cr(III), and Cs(I) had limits of detection (LOD) of 0.02, 0.005, 0.003, and 0.006  $\mu\text{g mL}^{-1}$ , respectively. Notably, the proposed optical chemosensor can detect selected ions in a human urine sample with a minimum concentration of 0.01  $\mu\text{g mL}^{-1}$ . Throughout this study, it was demonstrated that combining nano-based materials and DESs presents innovative and effective strategies for developing enhanced sensing devices. This approach results in hybrid devices that exhibit better signal-to-noise ratios, linearity, and selectivity.

Received 7th June 2025

Accepted 29th July 2025

DOI: 10.1039/d5ra04031k

rsc.li/rsc-advances

## 1. Introduction

Exposure to heavy metallic ions is one of the primary hazards in the workplace environment.<sup>1</sup> Heavy metals are widely dispersed throughout the environment due to their numerous industrial uses, exacerbating health hazard concerns.<sup>2–5</sup> Thousands of individuals are exposed to heavy metal ions in workplaces such as metalworking, construction, transportation, the chemical industry, and mining.<sup>6,7</sup> Exposure to these pollutants causes both acute and chronic toxicity, resulting in severe health impairments, including asthma, neurological disorders, bronchitis, chronic dermatitis, genetic damage, hypertension, hemoglobin changes, and damage to the liver, kidneys, and brain, as well as DNA damage and even cancer. The primary issue is that heavy metals are not metabolized in the body.<sup>7–10</sup>

In various industries, the easy detection and rapid evaluation of the levels of these ions is crucial to limiting their discharge

into the environment and avoiding adverse effects. This becomes especially important when these ions have very low toxic levels.<sup>11–13</sup> The significant costs associated with analytical techniques for detecting and measuring heavy metallic ions pose a major challenge for industries.<sup>14</sup> Therefore, the demand for new technology that is portable, affordable, and capable of rapid detection has increased. In light of this, developing a specific science that can quickly identify toxic metal ions is essential.

Atomic absorption spectrometry (AAS), inductively coupled plasma mass spectrometry (ICP-MS), electrochemical sensors, ultraviolet-visible spectrometry, and inductively coupled plasma optical emission spectrometry (ICP-OES) are the most common analytical techniques used to measure heavy metal ions.<sup>14–17</sup> Although these traditional methods have high accuracy, selectivity, and sensitivity and can detect low levels of analyte, they have some disadvantages in their use, such as expensive and complicated instruments, high running costs, time-consuming procedures, and the need for a trained operator.<sup>18–20</sup> Moreover, the use of these devices is not suitable for on-site and convenient detection of metal ions, as they are not portable. In recent decades, new methods have been

<sup>a</sup>Occupational Health Department, Isfahan University of Medical Sciences, Isfahan, Iran. E-mail: rismanchian@hlth.mui.ac.ir

<sup>b</sup>Pharmaceutical Analysis Research Center, Tabriz University of Medical Sciences, Tabriz, Iran. E-mail: hassanzadem@tbzmed.ac.ir



proposed to overcome these limitations, including sensors based on the various properties of nanostructured materials. These techniques aim to develop selective, sensitive, low-cost, and convenient detection platforms for monitoring various analytes in real samples.<sup>4,21–23</sup>

Sensors are one of these advanced methods. Sensors may be classified based on how they use signal-transduction mechanisms, such as field-effect transistor (FET), optical, and electrochemical sensors.<sup>24,25</sup> Optical sensors are a diverse group of those tools that use light to detect a variety of analytes. Optical sensors offer distinct advantages, including the ability to rapidly acquire signal readout, capture spatiotemporal imaging, and remotely detect target analytes.<sup>26,27</sup> Interestingly, the application of metal nanoparticles (NPs) on the structure of optical sensors led to their excellent performance in pollutant recognition.<sup>28–30</sup>

Silver (Ag) nano-crystals as engineered nanomaterials are used in a wide range of applications, including cosmetics, art, orthopedics, biomedicine, and optical sensors, due to their unique optical properties and the simplicity of the method of synthesis.<sup>14,31</sup> They interact strongly with visible light due to their localized surface plasmon resonance (LSPR).<sup>30,32–34</sup> The SPR band and the color absorbed by nanoparticles from visible light are strongly sensitive to characteristics such as particle size, shape, composition, distance between particles, state of self-assembly, agglomeration, and dielectric environment.<sup>35–37</sup> When silver nanoparticles are aggregated, the SPR expands, moves towards the lower wavelengths, and therefore decreases in intensity.<sup>35</sup> Interestingly, Ag nanostructures show superior plasmonic properties, even better than Au according to the theory of Mie.<sup>38</sup>

Triangular Ag nanoplates stand out among the various Ag nanocrystals developed so far because of their adjustable plasmonic properties.<sup>39</sup> These properties can be fine-tuned throughout the visible and near-infrared range by carefully controlling the aspect ratio of their structures.<sup>33,40,41</sup> So, these nanoplates were used for colorimetric sensing.<sup>40,42–44</sup>

Colorimetric chemical sensors are analytical methods that allow the detection of analytes by the naked eye by changing the color of the material.<sup>45</sup> The simplicity and availability of colorimetric tests make them a viable alternative to spectrometric systems. In addition, they can be easily observed with the naked eye or simply by using a readily available, affordable, and easy-to-use smartphone.<sup>45,46</sup> The colorimetric detection of metal ions is usually achieved by complexing the metal ions with appropriate chelating agents. Complex design not only guarantees selectivity but also makes it easier to detect colorimetric variation.<sup>47</sup> One challenge in using colorimetric sensors is that the reaction responsible for the color change occurs slowly,<sup>45</sup> and the color change caused by nanoparticles disappears after a limited time (maximum 60 minutes) at room temperature. This is because of the potential for evaporating the solvent, which may limit its use in the analysis process. This issue can be effectively addressed and solved by employing deep eutectic solvents (DESs).<sup>48,49</sup>

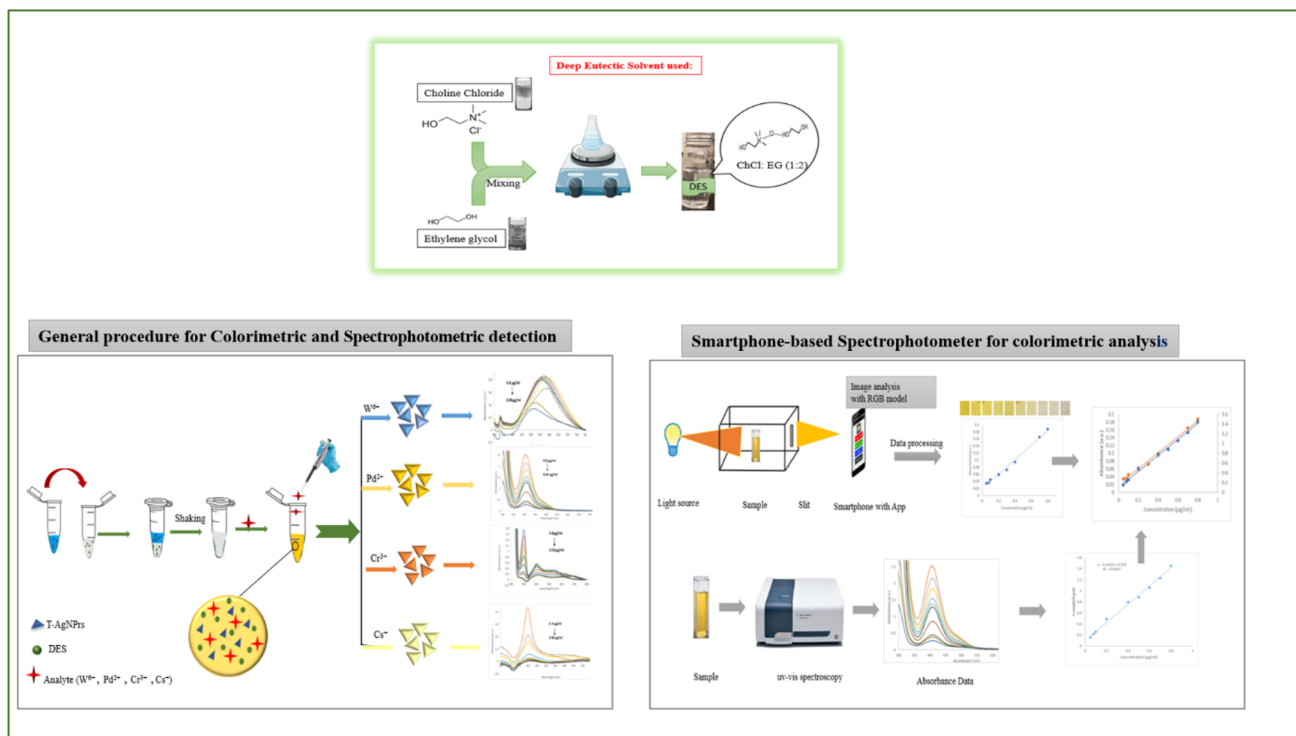
DES has received considerable attention as a safer solvent for a wide range of applications, especially as a green medium.<sup>50,51</sup>

Compared with traditional organic solvents, DES, as an alternative to ionic liquids (ILs), possesses the inherent advantages of ILs and demonstrates superiority in many aspects.<sup>52,53</sup> In particular, DES exhibits excellent stability under both temperature and chemical conditions and can be tailored to specific characteristics by altering its composition.<sup>54,55</sup> DES is also environmentally benign, featuring a low room temperature vapor pressure and minimal volatilization.<sup>56</sup> Its synthesis is inexpensive, typically straightforward, purer, and allows the preparation of materials with the desired density, polarity, and viscosity. Its notable biodegradability and remarkably low toxicity, along with the aforementioned properties, render them completely acceptable as green solvents.<sup>57</sup> Previously, DESs have been employed in various areas, including sample preparation, electrochemical analysis, chromatographic separation, modification of sorption materials, and synthesis.<sup>58</sup> According to recent research, DES can act as a chelating agent in colorimetric sensors for complex target metal ions, enhancing the selectivity of the analysis and generating color patterns for detection.<sup>46,47,59</sup> However, these studies did not investigate the potential high-SPR surface properties of noble metal nanoparticles using DESs in optical sensors. No research has been conducted to date to integrate NP materials with DES in chemical sensors. As a result, it remains a challenge to explore synergistic effects between these two components to achieve improved sensor performance for heavy metal ions. In this research, we have designed a new generation of optical sensors for the specific detection and determination of metal ions (W(IV), Pd(II), Cr(III), and Cs(I)). To date, the combination of DES with the plasmonic probe has not been utilized as an optical sensor for detecting metal ions. To the best of our knowledge, this marks the first time that T-AgNPs has been employed as a sensor probe in a DES medium without additives for the detection of metallic ions.

The assessment of metal ions in urine not only reflects individual health but also gives insight into potential environmental exposures. Many metals enter the human body through environmental sources, including water, food, and air pollution. Analyzing urine samples helps in understanding the correlation between environmental contaminants and health outcomes, thus guiding public health policies and interventions. For this purpose, the chemical colorimetric sensor was produced by dispersing T-AgNPs in a DES synthesized from choline chloride and ethylene glycol. UV-vis spectrophotometry quantified the resulting-colored complex of ions, and a smartphone-integrated photograph was taken for naked-eye detection and evaluation based on color change. Additionally, selected ions in human urine samples were determined using the proposed colorimetric probe.

In this study, we aim to compare spectral data with a smartphone-based spectrometer to create a portable and cost-effective device for the quick and accurate detection of W(VI), Pd(III), Cr(II), and Cs(I) in real samples. The smartphone-based colorimetric analysis system served as a visible spectrometer, allowing for the measurement of the absorbance of metal ions. This straightforward, affordable, and robust spectrometer design could enhance on-the-spot measurements. The device is





**Scheme 1** Schematic diagram for detecting  $W(vi)$ ,  $Pd(II)$ ,  $Cr(III)$ , and  $Cs(I)$  by T-AgNPs-DES as a colorimetric prob using a smartphone-based spectrophotometer and UV-visible spectroscopy.

inherently low-cost and portable, making it suitable for various field studies. Collecting and analyzing data is fast and easy. Despite the simplicity of the experiment, excellent results can be achieved. In terms of sensitivity, the performance of the smartphone-based spectrometer is comparable to that of commercial spectrometers. A good agreement was found between the smartphone-based spectrometer and the conventional spectrophotometer. Finally, the proposed method was tested by analyzing the candidate ion concentrations in real samples (human urine), yielding satisfactory sensitivity and accuracy. The limit observed in this study is lower, confirming the method developed as an appropriate alternative that can be easily reproduced by other researchers for the trace determination of  $W(vi)$ ,  $Pd(II)$ ,  $Cr(III)$ , and  $Cs(I)$ . The general steps of the study are illustrated in Scheme 1.

## 2. Materials and methods

### 2.1. Materials

All reagents are prepared from analytical grade chemicals without any purification. Silver nitrate ( $AgNO_3$ ), polyvinylpyrrolidone (PVP K, MW = 40 000), sodium borohydride ( $NaBH_4$ , 96%), hydrogen peroxide ( $H_2O_2$ , 30 wt%), and tri-sodium citrate (TSC) ( $Na_3C_6H_5O_7$ ) were acquired from Sigma-Aldrich (Ontario, Canada). The Stock standard solutions of ions ( $As(III)$ ,  $B(III)$ ,  $Fe(III)$ ,  $Ca(II)$ ,  $Te(IV)$ ,  $V(III)$ ,  $Sr(II)$ ,  $W(vi)$ ,  $Co(II)$ ,  $Zr(IV)$ ,  $Na(I)$ ,  $Mo(vi)$ ,  $Al(III)$ ,  $Ba(II)$ ,  $Cr(III)$ ,  $Pt(IV)$ ,  $Bi(III)$ ,  $Sn(II)$ ,  $Mn(II)$ ,  $Pb(II)$ ,  $Ni(II)$ ,  $Cs(I)$ ,  $Si(IV)$ ,  $Hg(II)$ ,  $Se(IV)$ ,  $K(I)$ ,  $Li(I)$ ,  $Zn(II)$ ,  $Mg(II)$ , and  $Pd(II)$ ) were purchased from Chemlab company

(Zedelgem, Belgium) at a concentration of  $1 \mu g \text{ ml}^{-1}$ . TA-AgNPs was synthesized according to our previous report<sup>20</sup> which was illustrated in Scheme 2.

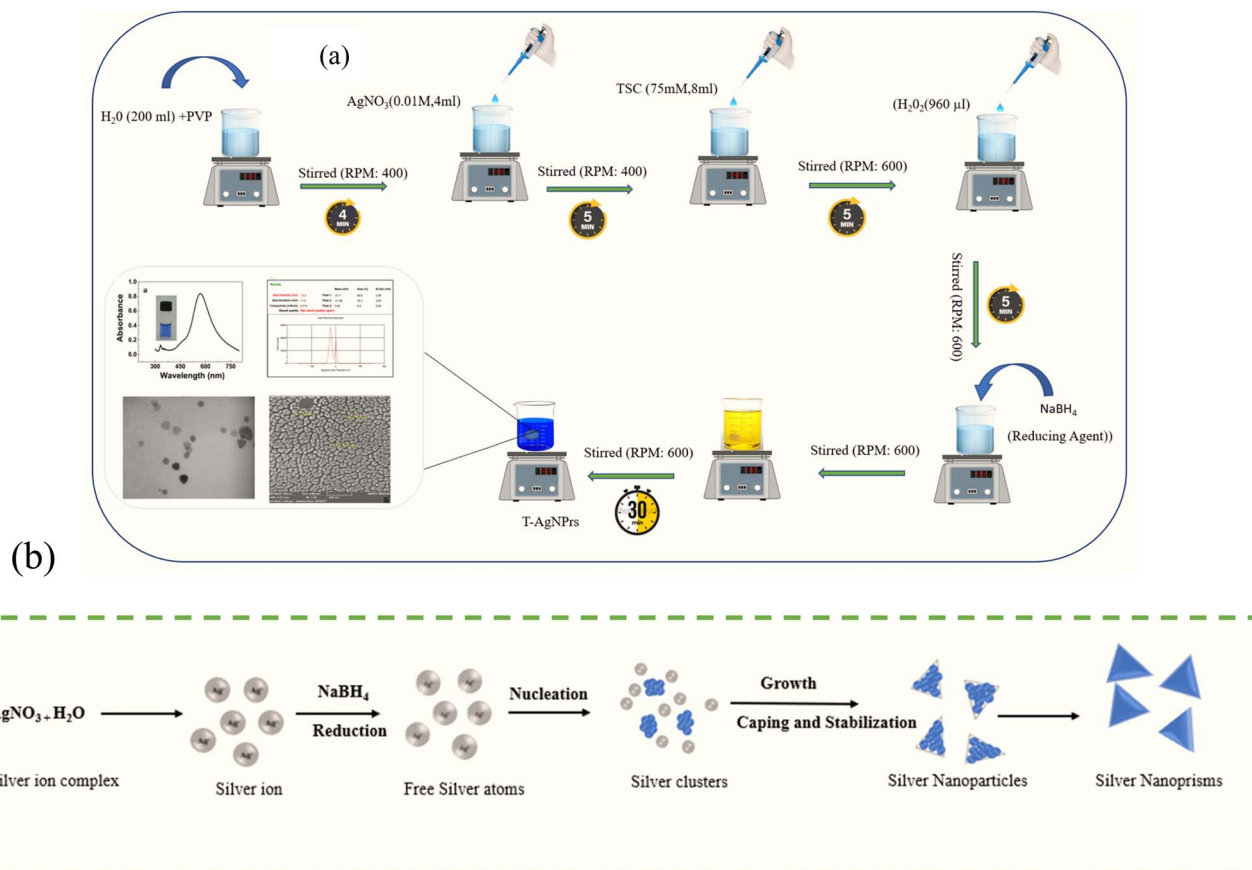
Working standard solutions were prepared fresh every day from stock solutions in DES. Choline chloride (ChCl) and ethylene glycol (EG) (>98%) were sourced from the Merck Co. (Darmstadt, Germany). Prior to the synthesis of DES, ChCl was dried in the oven for at least 4 h to guarantee a very low moisture content. All glassware was rinsed with distilled water after being washed with 5% detergent and 10% (v/v) nitric acid.

### 2.2. Instruments

Transmission electron microscopy (TEM; Adelaide, Australia) was used to investigate the size and internal structure of the synthesized Ag-nanostructure at a voltage of 200 kV. The diluted NPs were deposited on a copper grid to create the TEM image of the dispersed Ag-nanostructure.

The surface morphology and distribution of the synthesized Ag-nanostructures was evaluated with high-resolution field emission scanning electron microscopy (FE-SEM; Hitachi-Su8020, Czech Republic) at a voltage of 3 kV. Optical properties measurements were conducted with the ultraviolet-visible (UV-vis) spectrophotometer (A Shimadzu UV-1800) as a reference instrument for quantitative analysis, with a one-nanometer resolution using a quartz cell. The reaction solutions were scanned at a wavelength of 200–800 nm. In addition, absorbance measurements were made using smartphone-based spectroscopy for potential in-field applications. The zeta





Scheme 2 A schematic illustrating the synthesis process of silver nanoprisms (a). The proposed mechanism of producing silver nanoparticles (b).

potential and hydrodynamic size were also examined using dynamic light scattering (DLS) from Malvern Instruments Ltd (Zetasizer Ver. England, 7.11, MAL1032660). The Fourier-transform infrared (FT-IR) spectra was performed with the Nicolet IS 10 spectrometers (ThermoFisher Scientific Inc., Waltham, MA, USA). All the digital images in this work have been taken with a smartphone camera (Samsung Galaxy A54) under natural light.

### 2.3. Synthesis of deep eutectic solvents (DES)

The Hydrophilic DES<sub>s</sub> were synthesized by mixing quaternary ammonium salts (choline chloride) as a hydrogen bond acceptor (HBA) and with three hydrogen bond donors (HBDs), including ethylene glycol (ethaline), glycerol (glycerin), and urea in a ratio of 1 : 2 molar. Solid choline chloride was heated to ~70 °C to remove any water from the previous use. All DES synthesis methods were similar. For example, ethaline was chosen as the model DES, and the synthetic route is shown in Fig. S1 (see SI). ChCl and ethylene glycol in a 1 : 2 molar ratio (ChCl-EG, ethylene glycol) was added to the closed flask and heated at 80 °C under continuous magnetic stirring at 400 rpm until a clear and transparent liquid was formed. The colorless solution was cooled to room temperature and stored in a desiccator for future use. The FT-IR was used to further characterize ethaline (ChCl : EG, 1 : 2). In addition, to further

verify the successful synthesis of DES, a control experiment was conducted with FT-IR to characterize HBA and HBD before mixing. DES solvent was freshly prepared and used without further processing or dilution.

### 2.4. Preparation of colorimetric sensing platform (T-AgNPrs in the DES medium)

Metal ions were identified by integrating T-AgNPrs in the presence of DES as the colorimetric probe. The DES of ethaline was selected for further research. Initially, standard ion solutions, including As(III), B(III), Fe(III), Ca(II), Te(IV), V(III), Sr(II), W(VI), Co(II), Zr(IV), Na(I), Mo(IV), Al(III), Ba(II), Cr(III), Pt(IV), Bi(III), Sn(II), Mn(II), Pb(II), Ni(II), Cs(I), Si(IV), Hg(II), Se(IV), K(I), Li(I), Zn(II), Mg(II), and Pd(II) (each with a concentration of 1 µg ml<sup>-1</sup>), were added to the separate 2 ml microcentrifuge tubes. Afterward, the DES and T-AgNPrs were transferred in equal volume ratios to a microcentrifuge tube containing a standard ionic solution (1 : 1 : 1, v/v/v) to study the interaction of the optical probe with the analytes. After that, the solution was shaken by hand to create a homogeneous mixture. Human urine samples were obtained from the Tabriz University of Medical science, Tabriz, Iran, (ethic code: IR.MUI.RESEARCH.REC.1400.482). All experiments were performed in accordance with the guidelines of institute (Tabriz University of Medical science), and approved by the ethics committee at Tabriz University of Medical science,





Tabriz, Iran. Informed consents were obtained from human participants of this study.

### 2.5. Colorimetric detection

Colorimetric recognition was performed using a smartphone camera. This technology is used to monitor the stability of the color complexes and capture images of them. The images of the solution were taken under natural light using the Samsung A54 smartphone with a 50 MP camera. The solutions' color codes were assigned to the red, green, and blue (RGB) codes using the PhotoMetrix app to provide a universal colorimetric method. Subsequently, the Colorxs website was used to convert the assigned codes into color names.

### 2.6. Spectrophotometric detection

UV-vis spectrometry was used to quantify the metal ions at room temperature. For this, 500  $\mu\text{l}$  of T-AgNPrs was added to a centrifuge tube containing 500  $\mu\text{l}$  of DES and 500  $\mu\text{l}$  of standard ion solutions (total volume of 1.5 ml). After the solution was manually mixed for 30 seconds, absorption spectra of the final mixture were determined at regular intervals (0, 30, and 60 min) for optimization of reaction time. For all samples, the UV-vis spectra were recorded from 200 to 800 nm, and the graphs were carefully analyzed to compare results.

### 2.7. The design and fabrication of a smartphone-based spectrophotometer

The rectangular box (herein after referred to as the sample box) was designed to allow the passage of light through the sample. The area outside the box was covered to create an environment that effectively insulates the light from the surroundings. A hole corresponding to the diameter of the micro-tube is cut at the apex of the sample box. The sample box is then fitted with holes on both the front and the back. The front hole guides the smartphone camera to the solution, while the back hole allows light from the computer's LED screen to enter the sample. The distance between the smartphone and the sample box, as well as other components of the system, is kept at a constant level, which leads to increased accuracy. After all the necessary preparations were completed, the RGB analyzer application was launched on the smartphone.

### 2.8. Real sample evaluation

The proposed method was applied to the human urine sample without pretreatment. The results of the colorimetric measurements were recorded in a solution by smartphone and subsequently analyzed by a UV-vis spectrophotometer. An equal number of ions with T-AgNPrs-DES was individually combined with real samples.

### 2.9. Analytical study

First, the various concentrations of  $\text{W(IV)}$ ,  $\text{Pd(II)}$ ,  $\text{Cr(III)}$ , and  $\text{Cs(I)}$  were prepared by diluting the standard solution in a DES to construct the linear calibration curves. Afterwards, the T-AgNPrs was introduced into these solutions. The resulting

mixtures were then used for the measurement of the absorbance ratio ( $A_{\text{sample}}/A_{\text{prob}}$ ) by both commercial UV-vis spectroscopy and smartphone-based spectroscopy. Analytical signals obtained from both techniques were compared. Finally, calibration curves were generated for both trials by plotting absorbance ratio data against ion concentration. The low limit of quantification (LLOQ), limit of detection (LOD), limit of quantification (LOQ), and relative standard deviation (RSD%) were calculated for this study. The analytical signals derived from the two methods were contrasted.

## 3. Results and discussion

### 3.1. Characterization of synthesized materials

Ethaline ( $\text{ChCl}:\text{EG}$ , 1:2) was selected as the DES model to investigate T-AgNPrs spectral properties in the DES medium. T-AgNPrs were successfully characterized according to our previous reports.<sup>60,61</sup>

FTIR spectrometry was implemented to confirm the successful synthesis of the DES. FTIR spectra showed several absorption bands based on the DES composition ( $\text{ChCl}:\text{EG}$ ) and the hydrogen bonding between the ethylene glycol chloride and the  $\text{ChCl}$  anion. In the FTIR spectra, the O–H stretching vibration band typically occurs between 3200 and 3700  $\text{cm}^{-1}$  in FTIR spectra.<sup>62</sup> DES and its components, choline chloride and ethylene glycol, were subjected to FTIR analysis, as shown in Fig. S2 and S3 (see SI). The differential characteristics in the region between 400–1300  $\text{cm}^{-1}$  were remarkable, since this range corresponds to the fingerprint region of the spectrum. Analysis of the spectrum of pure choline chloride revealed absorption bands related to the O–H bond stretching and bending vibrations (3259 and 1480  $\text{cm}^{-1}$ , respectively) and the C–O bond stretching vibrations (1091  $\text{cm}^{-1}$ ). In addition, a stretching vibration of the C–N bond (951  $\text{cm}^{-1}$ ) was detected by the analysis. The pure ethylene glycol spectrum shows vibration signals of 3380, 1408, and 1041  $\text{cm}^{-1}$  for the stretching and bending of the O–H and C–O groups, respectively. The broadband at 3380  $\text{cm}^{-1}$  associated with the stretching vibration of the O–H functional group in ethylene glycol was found to shift to 3384  $\text{cm}^{-1}$  in DES, according to the FT-IR spectra. Reduced intermolecular hydrogen bonding between ethylene glycol molecules caused this shift towards a higher wave-number. Fig. S3 (see SI) shows a significant increase in spectral intensity in association with the OH functional group, which is attributed to hydrogen bonding formation by OH groups in the ethylene glycol and  $\text{ChCl}$  molecules, as reported in the literature.<sup>63</sup> The stretching vibrations of the C–O and the stretching and bending vibrations of the –OH were found to have some minor shifts. One possible explanation for these minor variations in the O–H and C–O peaks is the development of hydrogen bonding interactions between the HBD and HBA components. In the DES spectra, the  $\text{ChCl}$  features are visible. The stretching vibration of the C–N bond is represented by a sharp band in the DES spectra at 955  $\text{cm}^{-1}$ , which is slightly shifted compared to the  $\text{ChCl}$  pure spectra. Those results are consistent with other studies.<sup>64,65</sup> As was somehow expected, all these characteristic peaks were also found in the FT-IR spectrum, which confirmed



that the DES is successfully synthesized from choline chloride and ethylene glycol. This finding supports the idea that hydrogen bonding is necessary for the molecular interactions that take place in the DES system. The chemical stability of the prepared DES was also examined and characterized using FTIR for 28 days. The FTIR spectra (Fig. S2b (see SI)) indicated that the DES was stable.

### 3.2. Identify T-AgNPrs after mixing with DES

Zeta potential ( $Z_p$ ), electrical conductivity, hydrodynamic diameter (HD), and UV-vis spectroscopy were used to investigate of detection behavior of T-AgNPrs in the presence of DES as a sensing probe. The structure of the silver nanoprisms is a triangular sheet. According to earlier studies, silver triangular nanoprisms have high chemical activity at their corners and edges.<sup>66</sup> Therefore, the silver nanoprisms may undergo morphological changes as a result of a variety of external factors, including temperature, light from outside sources, time, and the addition of chemicals.<sup>55</sup>

Using UV-vis spectroscopy, the absorption characteristics of T-AgNPrs in the presence of DES were assessed. Fig. 1 graphically illustrates the absorption spectrum and the corresponding PRF shift of the T-AgNPrs in the DES mixture (T-AgNPrs-DES). Spectroscopic analysis of T-AgNPrs in combination with DES resulted in interesting results. Following the addition of silver nanoparticles to the DES, the characteristic peak absorption associated with the 450 and 336 nm wavelengths was shifted to the lower wavelength range (blue shift) while the maximum absorption peak of LSPR was shifted to 702 nm (red shift) with significantly reduced absorption (Fig. 2c) and the color of the nanoparticle changed from blue to colorless.

This significant shift can be attributed to differences in the distances of the particles and particle sizes of T-AgNPrs in the DES system. The SPR peak feature of the NPs in the presence of a DES could be due to energy transfer processes or changes in the electronic environment of the nanoparticles. However, understanding the effects of the DES on the PRF of colloidal NPs poses significant challenges. The physics governing the optical

response of solvent systems is fundamentally different from that of plasmonic materials.<sup>73</sup>

The zeta potential and surface conductance are essential interfacial electrokinetic properties for assessing the net surface charge and stability of nanoparticles. Synthesized nanoparticles will be almost stable if their  $Z_p$  is greater than +30 mV or less than -30 mV.<sup>67</sup> Higher levels of  $Z_p$  can prevent nanoparticle aggregation and increase particle size.<sup>68</sup> The charge on the surface of the colorimetric probe was evaluated by measuring the zeta potential. The  $Z_p$  of T-AgNPrs in the absence of DES was measured at -15 mV. Consequently, T-AgNPrs are stabilized in the aqueous dispersion despite the small zeta potential, due to significant electrostatic forces between T-AgNPrs coated with negatively charged molecules. After dissolving T-AgNPrs in DES, the average  $Z_p$  shifted to a positive value and reduced to 0.613 mV (Fig. S4 (see SI)). A reduction in zeta potential from -15 to 0.613 mV suggests that the anionic surface of the T-AgNPrs was nearly neutralized upon the addition of DES, correlating with diminished repulsive forces between colloidal particles. This decrease arises from various factors, including changes in the chemical composition of the surrounding medium (DES medium). It is assumed that in this system, T-AgNPrs react with chloride in the DES and precipitate an AgCl layer on the particles, which alters their zeta potential. The  $Z_p$  experiments showed that the molecules of DESs effectively dissolve metal nanoparticles. Conversely, the addition of AgNPrs to the studied DES led to changes in the liquid structure due to alterations in intermolecular forces, producing effective solvation around T-AgNPrs and consequently changing the intermolecular forces between the molecules constituting the DES. The characteristics of DES depend on the hydrogen bonding between the salt (choline chloride in this study) and the selected HBD.

The conductivity may be considered as an indicator of the presence of chemicals dissolved in the solution. Concentration of dissolved ion species that can freely move in the solution in proportion to the conductivity.<sup>69</sup> Experimental measurements have shown that DESs with high viscosity have lower conductivity, indicating an inverse relationship between conductivity and viscosity. This correlation can be explained by the simple fact that the consistency of the solvent has a direct effect on the movement of ion species within it.<sup>70</sup> The choline chloride and glycerol-based DES system has a high conductivity at room temperature ( $7160 \mu\text{S cm}^{-1}$ ) because of its high salt ratio.<sup>70,71</sup> The results of this study show that the colloidal system conductivity ( $714 \mu\text{S cm}^{-1}$ ) has significantly increased in the presence of DES ( $31\,000 \mu\text{S cm}^{-1}$ ). This increase is attributable to high salt concentration and an increased number of ions. The  $Z_p$  is also affected in colloidal systems with high conductivity. As the ion concentration increases, the  $Z_p$  decreases, resulting in a decrease in electrostatic attraction between particles. This decrease could result in more colloidal particle aggregation, which would affect the system's stability. The distribution of particle size (hydrodynamic diameter) by DLS is an effective method for understanding the occurrence of aggregation. Fig. S5 (see SI) illustrates that the average particle size of T-AgNPrs is approximately 20.4 nm and with

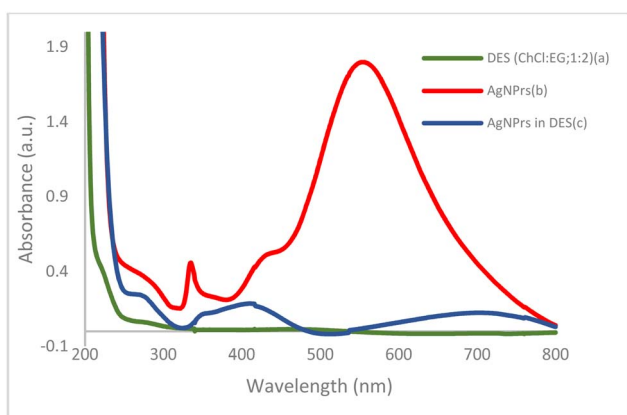


Fig. 1 The absorption spectrum of UV-vis and image of (a) T-AgNPrs, (b) DES (ChCl : EG; 1 : 2), (c) T-AgNPrs in DES at room temperature.



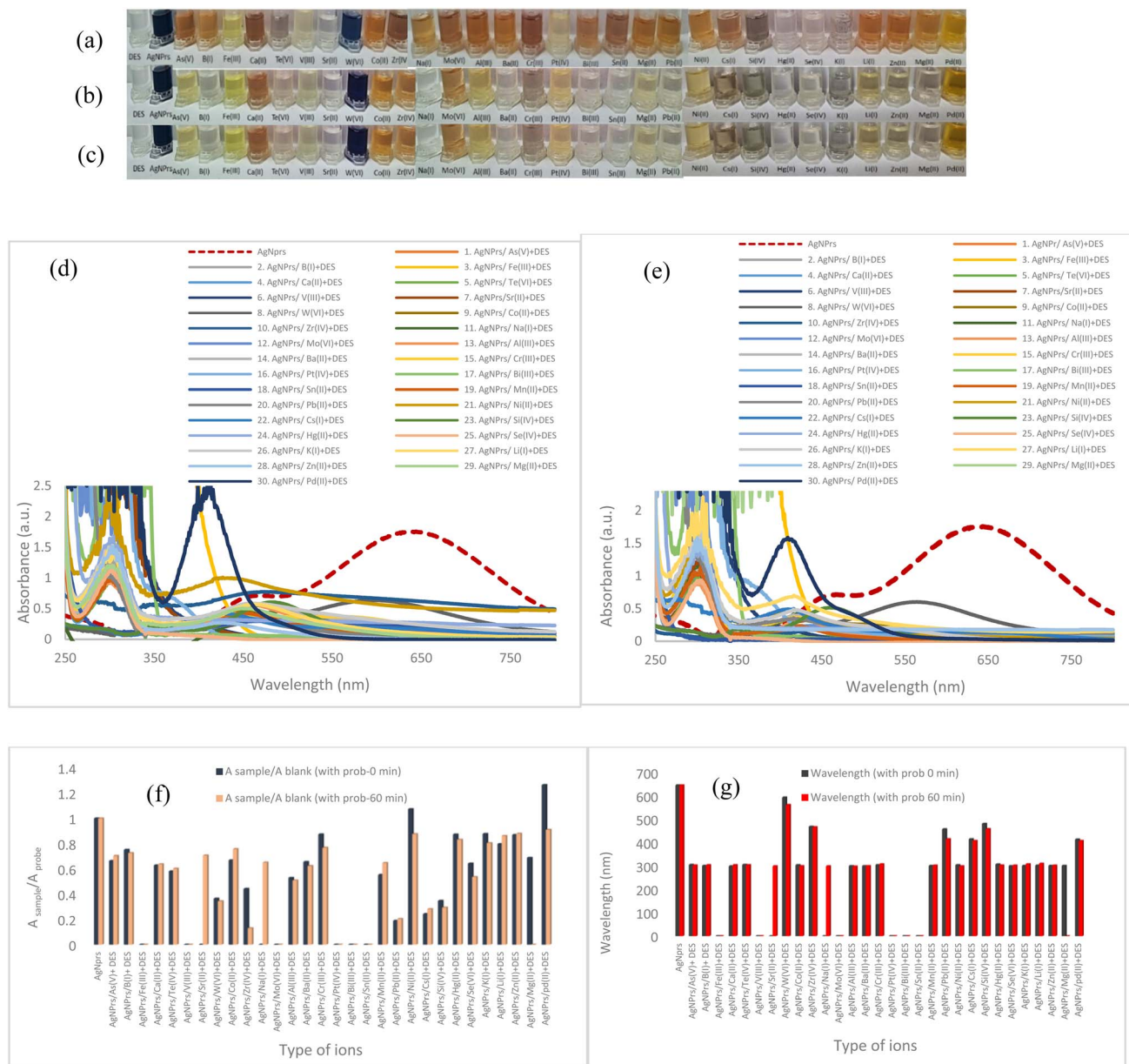


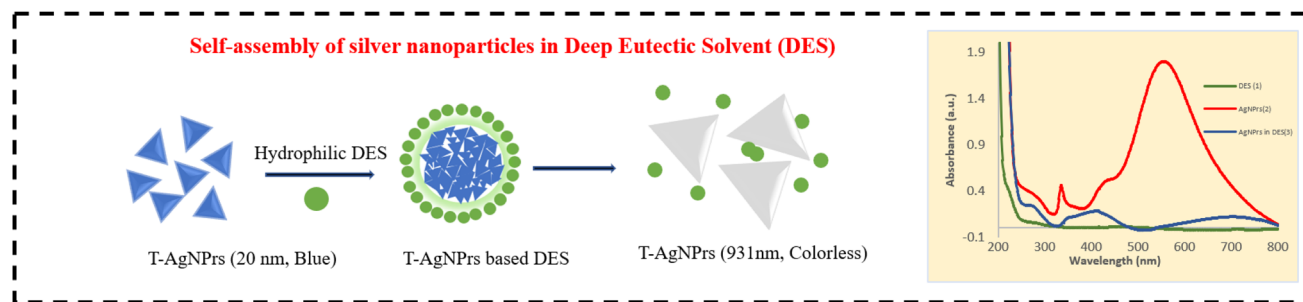
Fig. 2 Colorimetric detection of T-AgNPs in the presence of DES for the detection of different ions (1 : 1 : 1) (v/v/v) at three different incubation times: (a) 0, (b) 30, and (c) 60 min. The UV-vis spectra of the ions + DES + T-AgNPs (1 : 1 : 1) at two different incubation times: (d) 0 and (e) 60 min. Absorption intensity of T-AgNPs-DES with various ions at two different incubation times: (f) 0 and after 60 min. Wavelength shift of AgNPs-DES with various ions at two different incubation times: (g) 0 and after 60 min.

a polydispersity index (PDI) of 0.72. However, after adding DES to colloidal systems (Fig. S5 b (see SI)), the intensity was significantly decreased, and a new size distribution of 931.8 nm was formed (PDI = 0.464) after five minutes of interaction. This observation suggests a potential interaction between T-AgNPs and DES.

Therefore, MNPs in the DESs are expected to alter the liquid's structure due to changes in intermolecular forces that allow efficient solvation around MNPs. Therefore, one should anticipate changes in the intermolecular forces among the molecules forming the DESs, with the most significant alterations occurring in the solvation shells. The properties of DESs

fundamentally depend on the hydrogen bonding between the salt component (ChCl in this work) and the considered HBDs.<sup>46</sup> It can be hypothesized that the choline cation interacts with the T-AgNPs due to the negative charge on their surface, and Ag atoms or nanoparticles can move and co-aggregate within the DES bulk because of the electrostatic interactions (cation-anion) among the DES molecules. In principle, the growth process may occur *via* individual atom attachment or co-aggregation of primary nanoparticles. The nanoparticle co-aggregation process in the DES depends on the interplay between surface tension and viscosity. H. R. Ghenaatian *et al.* reported a comprehensive study of the interaction between





Scheme 3 Schematic representation self-assembly of silver nanoparticles in DES medium.

DESs and NMNPs. In this study, choline chloride (ChCl) is selected as a hydrogen bond acceptor (HBA), and urea is also chosen as a hydrogen bond donor (HBD) for forming the DES (ChCl:urea). Results indicate that ChCl:urea interacts primarily with nanoparticles *via*  $[\text{Cl}]^-$  anion ( $[\text{Cl}]^- \cdots \text{Mn}$ ) and nonconventional H-bonds of  $\text{C}-\text{H} \cdots \text{Mn}$  and  $\text{N}-\text{H} \cdots \text{Mn}$ . Research results indicated that interactions between  $[\text{Cl}]^- \cdots \text{Mn}$  are stronger than the nonconventional H-bond interactions, and that the nature of the interaction between  $[\text{Cl}]^- \cdots \text{Mn}$  is electrostatic, while the nonconventional H-bonds of  $\text{C}-\text{H} \cdots \text{Mn}$  and  $\text{N}-\text{H} \cdots \text{Mn}$  are of van der Waals. They did report evidence of the self-assembly and ordering of the metal NPs in DES.<sup>73</sup> In conclusion, the analysis of the endings of UV-vis spectroscopy, zeta potential, conductivity, and size distribution tests together suggest that T-AgNPs in the present DES medium are in a self-assembly state (see Scheme 3). Based on the results of the studies, hydrogen bonding is the main driving force for the formation of self-assembly.<sup>72</sup> The mechanism of aggregation is attributed to the templating nature of the DES and the forces of physical interaction between the T-AgNPs and the DES.

### 3.3. Application of T-AgNPs-DES as a sensing platform

**3.3.1 Specific detection.** Specificity in detecting metallic cations and anions is a key characteristic of appropriate probe systems. For the analytical assessment of optical chemo sensors, one of the most crucial factors is specific detection.<sup>74</sup> Using a mixture of T-AgNPs and DES as a sensing platform, an individual experiment was conducted on each of the element ions to examine the specific detection of the target metal ion in the sample solution. Therefore, sensing the system was utilized to detection of metals ions with different valences, *i.e.*, ( $\text{As}(\text{III})$ ,  $\text{B}(\text{III})$ ,  $\text{Fe}(\text{III})$ ,  $\text{Ca}(\text{II})$ ,  $\text{Te}(\text{IV})$ ,  $\text{V}(\text{III})$ ,  $\text{Sr}(\text{II})$ ,  $\text{W}(\text{VI})$ ,  $\text{Co}(\text{II})$ ,  $\text{Zr}(\text{IV})$ ,  $\text{Na}(\text{I})$ ,  $\text{Mo}(\text{II})$ ,  $\text{Al}(\text{III})$ ,  $\text{Ba}(\text{II})$ ,  $\text{Cr}(\text{III})$ ,  $\text{Pt}(\text{IV})$ ,  $\text{Bi}(\text{III})$ ,  $\text{Sn}(\text{II})$ ,  $\text{Mn}(\text{II})$ ,  $\text{Pb}(\text{II})$ ,  $\text{Ni}(\text{II})$ ,  $\text{Cs}(\text{I})$ ,  $\text{Si}(\text{IV})$ ,  $\text{Hg}(\text{II})$ ,  $\text{Se}(\text{IV})$ ,  $\text{K}(\text{I})$ ,  $\text{Li}(\text{I})$ ,  $\text{Zn}(\text{II})$ ,  $\text{Mg}(\text{II})$ ,  $\text{Pd}(\text{II})$ ). All the mentioned cations were examined at a concentration of  $1 \mu\text{L ml}^{-1}$ . Fig. 2a–c shows the color changes that happened when the individual ions were mixed. These observations were recorded immediately following the reaction (0 min) and again at interval time of 30 and 60 min. Additionally, the absorption spectra of T-AgNPs-DES with various ions present, along with the corresponding wavelengths ( $\lambda_{\text{max}}$ ) and absorption intensities, are displayed in Fig. 2.

The results shown in Fig. 2 demonstrate that T-AgNPs can specifically detect  $\text{W}(\text{VI})$ ,  $\text{Pd}(\text{II})$ ,  $\text{Cr}(\text{III})$ , and  $\text{Cs}(\text{I})$  ions in the presence of DES under optimal conditions with 60 minutes of incubation and  $30^\circ\text{C}$ . Colorimetric results also produced blue, orange, purple (light taupe), and lion coloring complexes for  $[\text{DES}/(\text{T-AgNPs}-\text{W}(\text{VI})$ ,  $\text{Pd}(\text{II})$ ,  $\text{Cr}(\text{III})$ , and  $\text{Cs}(\text{I}))$ , respectively, indicating that these ions may interact with T-AgNPs in the presence of the DES. Therefore, the naked-eye colorimetric method could selectively detect  $\text{W}(\text{VI})$ ,  $\text{Pd}(\text{II})$ ,  $\text{Cr}(\text{III})$ , and  $\text{Cs}(\text{I})$  through the color alternation of the T-AgNPs-DES mixture. The extent and intensity of the LSPR-associated changes in  $\text{W}(\text{VI})$ ,  $\text{Pd}(\text{II})$ ,  $\text{Cr}(\text{III})$ , and  $\text{Cs}(\text{I})$  ions were confirmed by UV-vis spectrophotometer (Fig. 2). Interestingly, a hypochromic shift (shorter wavelength) was observed when  $\text{W}(\text{VI})$ ,  $\text{Pd}(\text{II})$ ,  $\text{Cr}(\text{III})$ , and  $\text{Cs}(\text{I})$  ions were increased in the reaction medium; with blue shifts at 563, 411, 310, and 410 nm, respectively. It should be noted that the LSPR band ( $\lambda_{\text{max}}$ ) at 300 nm was observed for other metal ions, which didn't produce a coloring complex. The calorimetry experiments without NPs and competitive experiments (absorbance and wavelength) were performed with and in two reaction times (Fig. S6 and S7 (see SI)). The absorption ratio ( $A_{\text{sample}}/A_{\text{blank}}$ ) for all metal ions examined is given in Fig. S8 (see SI).

**3.3.2 Sensing tests.** This section begins with an exploration of the UV-vis spectra of silver nanoparticles. UV-vis is the gold standard for quantitative analysis of chemical compounds undergoing an electronic transition from ground to excited state through energy source absorption. Most metals cannot be analyzed by UV-vis because they are colorless; therefore, they need to be treated with organic dyes, ligands, or chromophores. It is believed that three main factors influence the plasmon resonance of the particles and, therefore, the absorption: the surrounding solvents, the T-AgNPs aggregation, and the ion binding to the surface of the nanoprobe.<sup>75</sup>

The UV-vis absorption spectra of tungsten in the sensing probe showed a new LSPR band at approximately 563 nm and 340 nm because the NPs' plasmon characteristics changed due to the presence of the analyte. As shown in Fig. 3, T-AgNPs-DES exhibits no color. Upon completion of the reaction between the probe and tungsten, the solution changes color to blue. Additionally, the SPR band of T-AgNPs decreased from 650 nm to 415 nm upon the addition of palladium ions to the system. Moreover, the solution's color immediately changes to orange due to the agglomeration of T-AgNPs with palladium in the





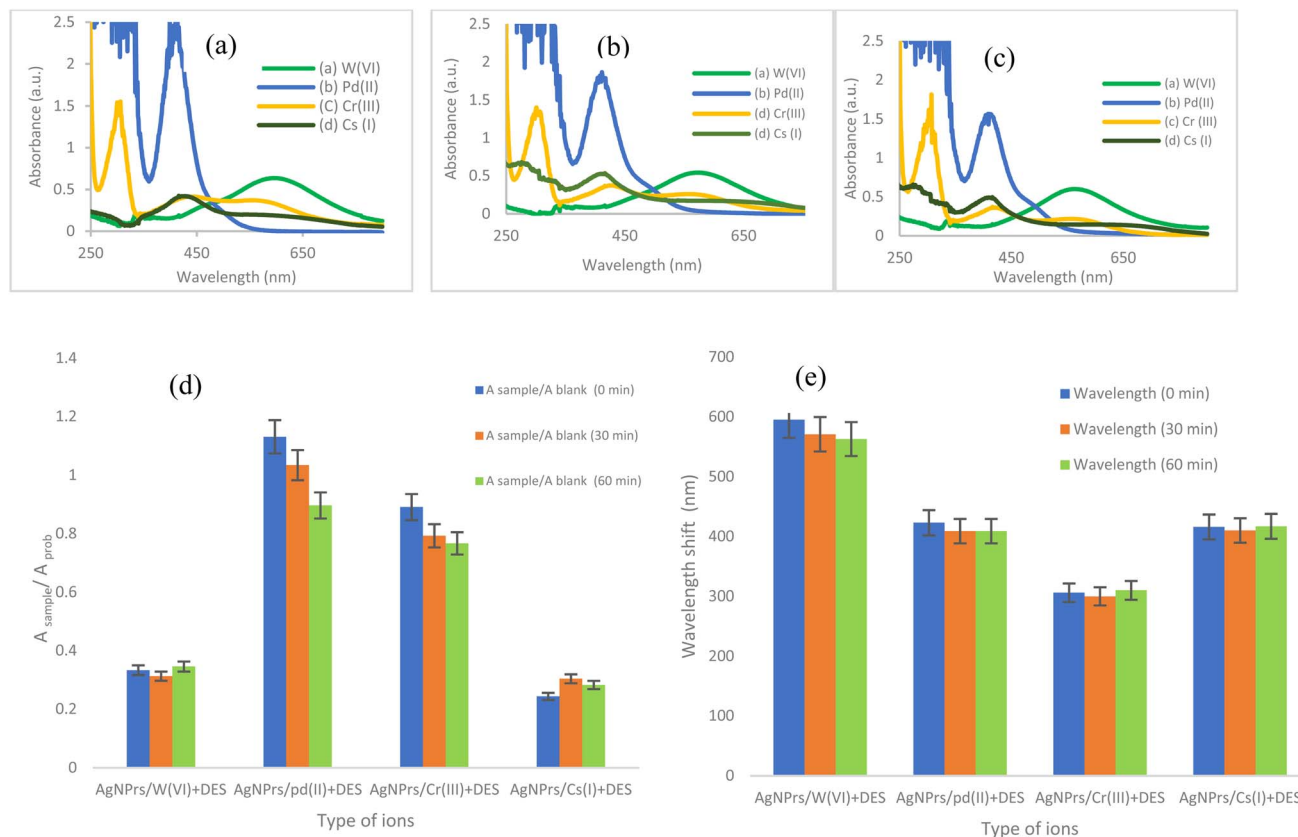


**Fig. 3** The UV-vis spectra of the interaction between T-AgNPs-DES with candidate ions [W(VI), Pd(II), Cr(III), and Cs(I)] in 0 (a), 30 (b), and 60 min (c) of incubation time. The related histogram of the position of shifted LSPR peaks versus candidate ions [W(VI), Pd(II), Cr(III), and Cs(I)] in 0, 30, and 60 min of incubation time (d). The related histogram of the absorbance intensity versus candidate ions [W(VI), Pd(II), Cr(III), and Cs(I)] in 0, 30, and 60 min of incubation time (e).

presence of the DES medium. Similarly, when T-AgNPs-DES interacted with chromium ions, a blue shift in the SPR absorbance band was recorded by UV-vis, with three new bands emerging at 306 nm (weak), 425 nm (medium), and 570 nm (strong), alongside the solution changing from colorless to Persian orange. When cesium ions are present in the reaction system, the formation of the complex DES/AgNPs [Cs(I)] caused significant shifts in the absorbance band of the SPR to 410 nm and also changed the color from colorless to a lion color; this may indicate alterations in the optical or chemical properties of the solution (See Fig. 2). The shift of the absorption band towards shorter wavelengths (blue shift) upon exposure to these ions indicates higher energy electronic transitions due to the complexes formed with T-AgNPs in the DES medium.<sup>76</sup> After 60 minutes of reaction time between the ions and NPs in the presence of DES, a slight discoloration of the solution was noted.

Another important parameter in optical sensing is the reaction time. As shown in Fig. 3, the wavelength shift remained almost constant with an increase in incubation time to 60 minutes, and the intensity of the absorption peak did not change significantly. Therefore, all measurements were performed with a 5 min of incubation time. The presence of the analyte leads to a dielectric change manifested as a change in

color as well as in the position (wavelength) and intensity of absorption (Abs). Thus, the peaks observed for the candidate metal ions can be attributed to the coordination of the metal ions with the silver atoms of NPs in the presence of DES.

DLS is employed to monitor the zeta potential, average particle size, conductivity, and polydispersity index of T-AgNPs after the addition of ionic solutions for the study of changes in nanoparticles in the presence of the DES. After adding W(VI), Pd(II), Cr(III), and Cs(I) ions to the T-AgNPs-DES (1 : 1 : 1 volume ratio), the mixture solution was incubated at ambient temperature for 60 minutes to complete the reaction. Table 1 shows how the  $Z_p$ , HD, conductivity, and polydispersity index of T-AgNPs changed over time for each of the aforementioned ions at various incubation times (0 and 60 min).

Table 1 shows that T-AgNPs exhibited high zeta potential due to a high surface charge, as the reference system. Importantly, the zeta potential decreased in the first few minutes after adding the ions along with DES as the particles interacted with the surrounding medium. For example, the  $Z_p$  of T-AgNPs, which was  $-15$  mV in the reference system, became  $0.995$  mV just after adding Pd(II) and decreased rapidly in the initial reaction phase. The decrease of the  $Z_p$  from  $-15$  to  $0.995$  mV indicates that the ionic strength system has increased in the early stages of the reaction, zeta potential also decreased for



**Table 1** Zeta potential, conductivity, average particle size distribution, intensity, and polydispersity index values for T-AgNPrs with metal ions in the presence of DES

Sample	Zeta potential (mV)	Conductivity (mS cm <sup>-1</sup> )	Average particle size distribution ( <i>d</i> nm)	Polydispersity index (PDI)
T-AgNPrs	−15.3	0.714	20.40	0.727
T-AgNPrs-DES	0.613	31.3	931.8	0.464
T-AgNPrs-DES + W <sup>6+</sup> (0 min)	−0.966	48.6	42.02	0.443
T-AgNPrs-DES + W <sup>6+</sup> (60 min)	−4.79	47.2	442.4	0.324
T-AgNPrs-DES + Pd <sup>2+</sup> (0 min)	0.995	74	472.2	1
T-AgNPrs-DES + Pd <sup>2+</sup> (60 min)	−4.05	67.2	506.6	0.529
T-AgNPrs-DES + Cr <sup>3+</sup> (0 min)	5.04	78.5	253.1	0.266
T-AgNPrs-DES + Cr <sup>3+</sup> (60 min)	−0.658	69.8	531.7	0.450
T-AgNPrs-DES + Cs <sup>+</sup> (0 min)	1.29	48.9	449.5	0.418
T-AgNPrs-DES + Cs <sup>+</sup> (60 min)	6.71	47.4	963	0.716

W(vi), Cr(III), and Cs(I) ions (Table 1). Consequently, the decrease in the zeta potential can be attributed to the increase in the ionic strength of the system, increasing agglomeration of the T-AgNPrs (decreasing particle separation).<sup>77</sup> The behavior and performance of the colloid particles in the sensing system can be greatly significantly by high salt concentrations and a high ion count in DES. After adding the mentioned ions to the colorimetric probe, the  $Z_p$  changed to a more positive value, indicating that the ions have been complexed by the liquid colorimetric probe ([T-AgNPrs-DES]/ion).

As aggregation is a dynamic process, its influence on the zeta potential can change over time.<sup>78</sup> To examine this issue,  $Z_p$  measurements were conducted at two different times (Table 1). The results of the change in zeta potential as a function of time are presented in Table 1 and Fig. S9 (see SI). As shown in Table 1, for 60 minutes, W(IV) maintains a negative  $Z_p$  between −0.966 and −4.79. In contrast, Pd(II) initially displayed a positive potential of 0.995 mV at 0 minutes of reaction time, which then shifted to approximately −4.05 mV after 60 minutes. The effect of Cr(III) on the zeta potential is 5.04 during the first 0 minutes, but decreases to approximately −0.658 after 60 minutes. After adding Cs(I) to the reaction system,  $Z_p$  increases from 1.29 to 6.71 over 60 minutes. Thus, one can consider that the ion affects the zeta potential of the probe in comparison to the reference system. This investigation found that the addition of ions to the sensing system correlates perfectly with the decreased zeta potential. The DLS data also supports this observation (Fig. S10–S13 (see SI)).

Conductivity increased due to high ion concentration and the hydrogen bond network in the presence of DES, as shown in the conductivity results in Table 1. In colloidal systems with high conductivity,  $Z_p$  reduction can lead to the formation of aggregate particles. Size distribution profiles (preferably by intensity) were also assessed using DLS. The radius of the synthesized NPs is 20.4 nm, as illustrated in Fig. S4a (see SI). The interaction of the analyte with the T-AgNPrs in the presence of DES at two distinct reaction times (0 and 60 min) was also examined by analyzing the size distribution of T-AgNPrs in the presence of candidate ions. An increase in particle size, along with a high hydrodynamic radius, indicates that NPs are accumulating in the presence of the analyte (Table 1 and Fig. S10–

S13 (see SI)). These findings demonstrate that the self-assembly process that produces aggregates of MNP is primarily time-dependent. The co-aggregation of T-AgNPrs-DES with ions was confirmed by results from DLS. These results are particularly interesting, as the dispersion characteristics of nanoparticles differ significantly depending on the type of dispersant used. This will have a substantial effect on the zeta potential values of T-AgNPrs and the SPR behavior.

### 3.4. Investigations of the interactions between AgNPrs-DES and metal ions

The previous section demonstrated that the addition of metal ions (W(vi), Pd(II), Cr(III), and Cs(I)) to T-AgNPrs in the presence of DES results in the formation of a T-AgNPrs cluster. This section investigates whether the cluster formation process is an aggregation (irreversible) or agglomeration (reversible). This is achieved by mixing T-AgNPrs with the metal ions listed above in the DES medium. The UV-vis spectra were recorded and compared at different response times: 0, 30, and 60 minutes after the end of the ion detection procedure. Spectra result of the mixtures at these reaction times are given in Fig. 4. Based on this finding, it is concluded that T-AgNPrs clusters are irreversibly aggregated when in the medium DES. Aggregation provides confidence for determining metal ions based on the nanoparticle, as it ensures that no cluster de-agglomerates within the measurement time. Moreover, due to the irreversible aggregation process, the measured responses accurately represent the concentration of metal ions in the samples.

### 3.5. Method validation

Important analytical parameters were assessed to confirm the analytical performance of the T-AgNPrs-DES as an optical sensor for all the analytes analyzed using UV-vis spectrophotometry. These parameters included regression equations, linearity, limit of detection (LOD), limit of quantification (LOQ), lower limit of quantification (LLOQ), and relative standard deviation (RSD). The most crucial factor in determining the lowest concentration that can be measured with adequate precision and accuracy for a recently developed analytical technique is sensitivity. The sensitivity of developed analytical



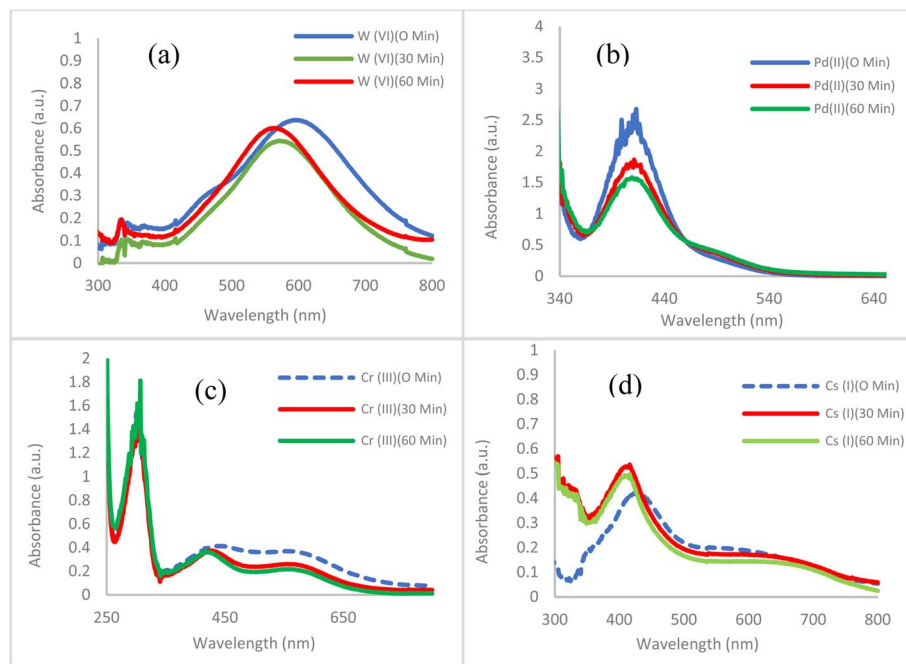


Fig. 4 UV-vis spectra of the mixtures of [T-AgNPrs-DES] + metal ions ( $1 \mu\text{g mL}^{-1}$ ): [T-AgNPrs-DES] +  $W^{6+}$  (a); [T-AgNPrs-DES] +  $Pd^{2+}$  (b); [T-AgNPrs-DES] +  $Cr^{3+}$  (c); [T-AgNPrs-DES] +  $Cs^+$  (d) at different reaction times. Red and green lines designate the spectra of the mixtures of the optical probe-ion reaction after 30 and 60 min, respectively. The blue dashed line shows the spectrum of fresh [T-AgNPrs-DES] + metal ions.

techniques is often compared using the quantification LOQ and LOD. These represent the lowest concentrations of an analyte in a sample that can be detected and quantified, respectively.

Thus, UV-vis spectrophotometry was used to determine the adsorption and ion concentration relationship, and the absorbance ratio ( $A_{\text{sample}}/A_{\text{prob}}$ ) was used to create the calibration

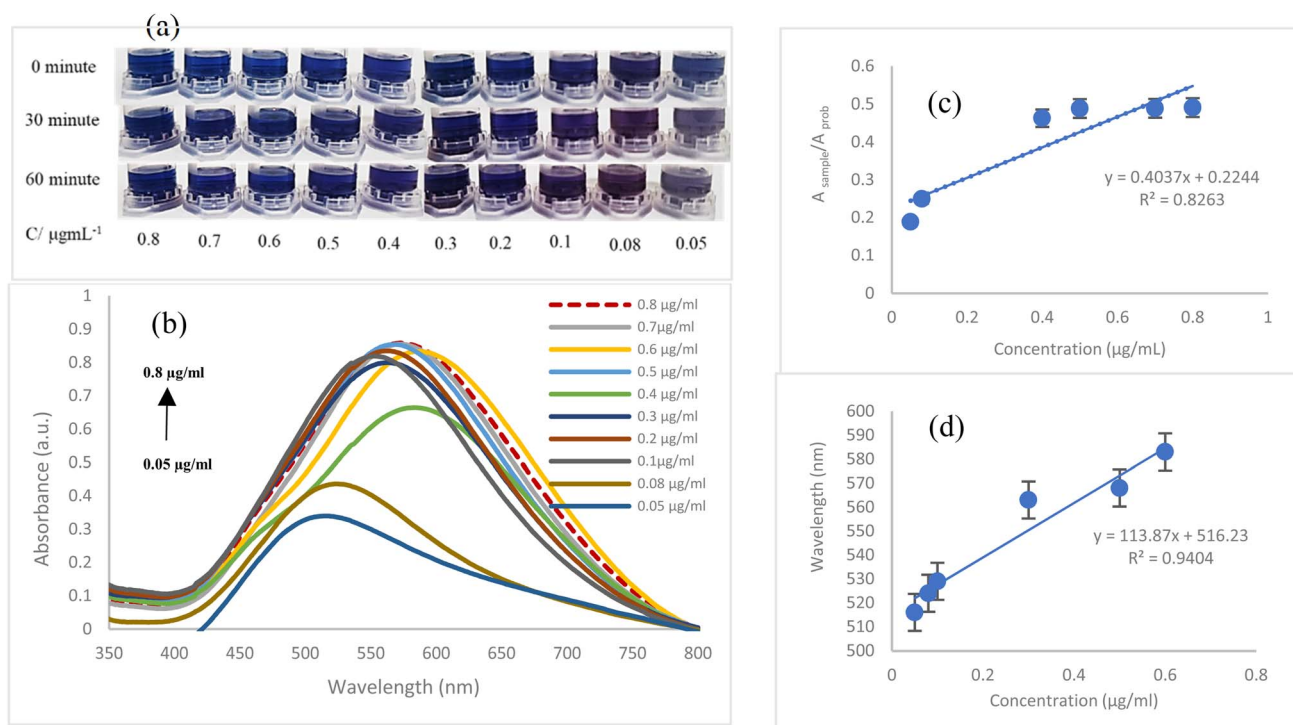
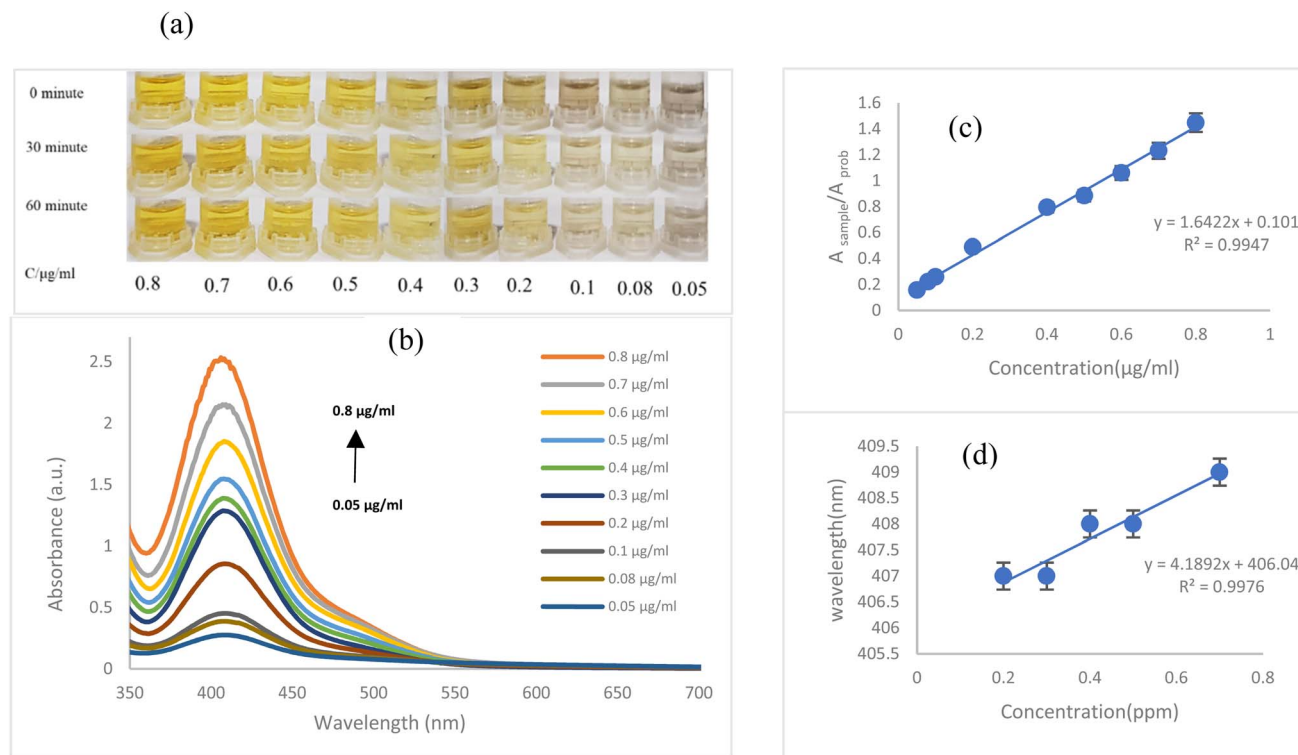


Fig. 5 Photographic images of T-AgNPrs-DES spiked with  $W^{(vi)}$  of different concentrations at various incubation times (0, 30, and 60 min) with a volume ratio of 1 : 1. (a) Absorption spectrum peak of T-AgNPrs at different concentrations of  $W^{(vi)}$  in the presence of DES (1 : 1 v/v ratio) after 60 min (b). The calibration curve of absorption ratios ( $A_{\text{sample}}/A_{\text{prob}}$ ) versus  $W^{(vi)}$  concentrations (c) and the wavelength dependence on  $W^{(vi)}$  concentrations (d) from 0.05 to 0.8  $\mu\text{g mL}^{-1}$ .



**Fig. 6** Photographic images of T-AgNPrs-DES spiked with Pd(II) of different concentrations at various incubation times (0, 30, and 60 min) with a volume ratio of 1 : 1 (a). Absorption spectrum peak of T-AgNPrs at different concentrations of Pd(II) in the presence of DES (1 : 1 : 1 v/v/v ratio) after 60 min (b). The calibration curve of absorption ratios ( $A_{\text{sample}}/A_{\text{prob}}$ ) versus Pd(II) concentrations (c) and the wavelength dependence on Pd(II) concentrations (d) from 0.05 to 0.8  $\mu\text{g ml}^{-1}$ .

curve. The sensing probe was combined with different concentrations of ion standard solutions in a volume ratio of 1 : 1, v/v, and then the change in the color intensity of the liquid probe was photographed at various incubation times (0, 30, and 60 minutes). The LOD and LOQ were computed by the standard deviation of the response (SD) and the slope of the calibration curve ( $m$ ) according to the equation  $3 \text{ SD}/m$  and  $10 \text{ SD}/m$ , respectively. The LLOQ is the analyte concentration in a sample that can be quantitatively identified with an acceptable level of precision [relative standard deviation (RSD) < 20 percent]. RSD is computed as standard deviation/mean  $\times 100$  percent, which is also referred to as the coefficient of variation (CV).

Optical images obtained of the various concentrations of metal ions ( $\text{W}(\text{vi})$ ,  $\text{Pd}(\text{II})$ ,  $\text{Cr}(\text{III})$ , and  $\text{Cs}(\text{I})$ ) in the sensing system, corresponding to the peaks of the absorption spectrum and the calibration curve of the absorption ratios ( $A_{\text{sample}}/A_{\text{blank}}$ ) are shown in the Fig. 5–8.

The effect of  $\text{W}(\text{IV})$  concentration on the color of the prob was investigated by preparing various concentrations of  $\text{W}(\text{IV})$  (0.05–0.8  $\mu\text{g ml}^{-1}$ ) in DES. Results show that there are no noticeable differences in color between 0.05 and 0.8  $\mu\text{g ml}^{-1}$  of  $\text{W}(\text{vi})$ , and the color of the solutions does not change significantly with passing time (over the 60 minutes after the reaction time). Therefore, it is considered that the concentration difference of  $\text{W}(\text{IV})$  in the concentration range of 0.05–0.8  $\mu\text{g ml}^{-1}$  with a reaction time of 5 min. It is not visible to the naked eye.

The absorption spectrum of the  $[\text{T-AgNPrs-DES}/\text{W}^{6+}]$  complex with  $\lambda_{\text{max}} = 573 \text{ nm}$  is displayed in Fig. 5b. The increased absorption ratios are in coordination with the  $\text{W}^{6+}$  concentration increase. Regression equation  $\text{Abs} (A_{\text{sample}}/A_{\text{prob}}) = 0.4037C_{(\text{W}^{6+})} + 0.2244$  ( $R^2 = 0.8263$ ) shows linearity between 0.05–0.8  $\mu\text{g ml}^{-1}$ . The LOD, LOQ, and LLOQ of the proposed method were 0.02  $\mu\text{g ml}^{-1}$ , 0.07  $\mu\text{g ml}^{-1}$ , and 0.05  $\mu\text{g ml}^{-1}$ , respectively. The wavelength of the third LSPR peak prob is plotted against the  $\text{W}(\text{IV})$  concentration with the regression equation  $\lambda = 113.87C_{(\text{W}(\text{IV}))} + 516.23$  ( $R^2 = 0.9404$ ).

The optical system (T-AgNPrs-DES) was used to study the concentration effect of Pd(II) in the range of 0.05–0.8  $\mu\text{g ml}^{-1}$ . The absorption spectra of  $[\text{T-AgNPrs-DES}/\text{Pd}(\text{II})]$  as well as the change in the color intensity of the suggested optical probe at different  $\text{Pd}^{2+}$  concentrations are shown in Fig. 6a and b. The results indicate that there is a clear color difference between 0.05 and 0.8  $\mu\text{g ml}^{-1}$  of Pd(II), and the color of the solution is not significantly changed after 30 minutes of reaction time. Therefore, the difference in  $\text{Pd}^{2+}$  concentration between 0.05 and 0.8  $\mu\text{g ml}^{-1}$  is visible to the naked eye with a reaction time of 30 min. The relationship between the concentration of Pd(II) and the wavelength of  $[\text{T-AgNPrs-DES}/\text{Pd}(\text{II})]$  complex ( $\lambda_{\text{max}} = 406 \text{ nm}$ ) is plotted in the range of 0.05–0.8  $\mu\text{g ml}^{-1}$ . The regression equation for this range of Pd(II) concentration is  $\lambda = 4.1892C_{(\text{Pd}(\text{II}))} + 406.04$  with  $R^2 = 0.9276$ . The absorbance ratio of Pd(II) standard solutions (from 0.05 to 0.8  $\mu\text{g ml}^{-1}$ ) with good





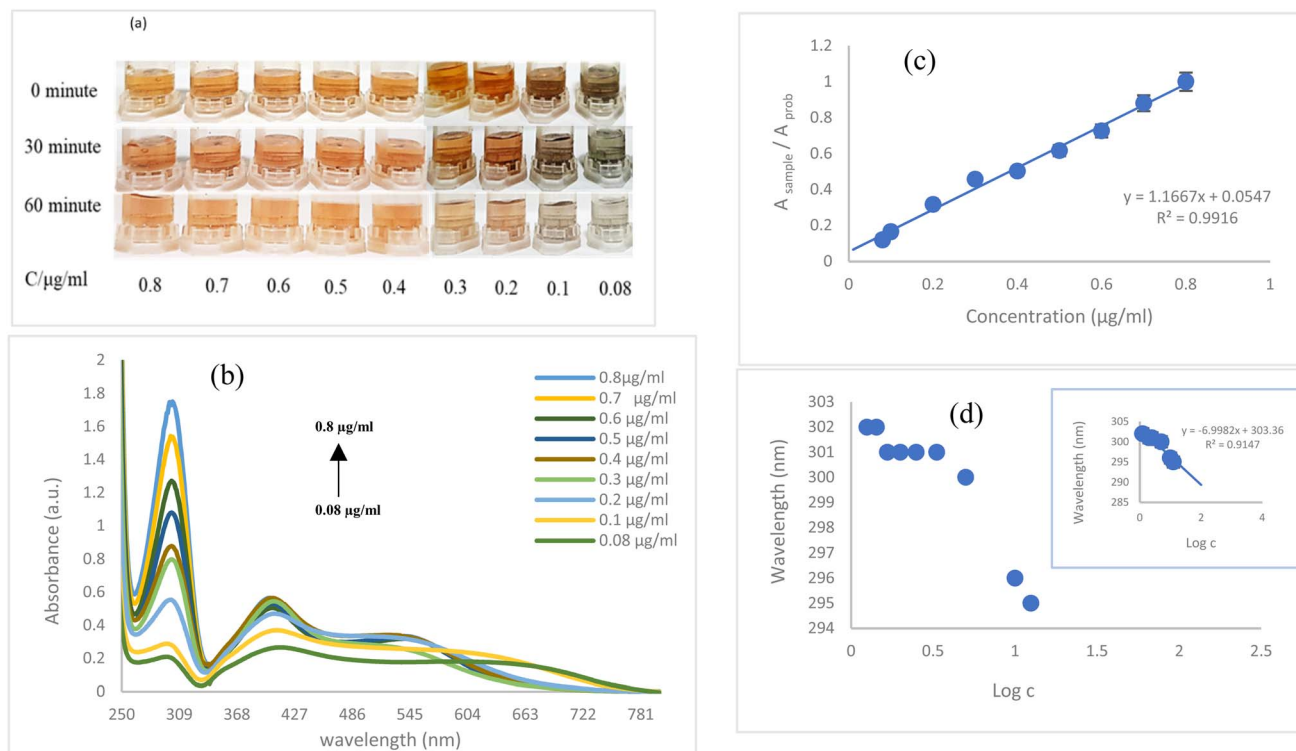


Fig. 7 Photographic images of T-AgNPrs-DES Cr(III) of different concentrations at various incubation times (0, 30, and 60 min) with volume ratio 1 : 1 (a). Absorption spectrum peak of T-AgNPrs at different concentrations of Cr(III) in the presence of DES (1 : 1 v/v ratio) after 60 min (b). The calibration curve of absorption ratios ( $A_{\text{sample}}/A_{\text{prob}}$ ) versus Cr(III) concentrations (c) and the wavelength dependence on Cr(III) concentrations (d) from 0.08 to 0.8  $\mu\text{g ml}^{-1}$ .

levels of linearity as the metal ion concentration increased, according to the linearity calibration curve (Fig. 6b). The  $R^2$  value of the created calibration curve, which was 0.9947 (regression equation,  $\text{Abs} (A_{\text{sample}}/A_{\text{prob}}) = 1.6422C_{\text{Pd(II)}} + 0.101$ ), confirmed the linearity of the proposed method (regression equation,  $\text{Abs} (A_{\text{sample}}/A_{\text{prob}}) = 1.6422C_{\text{Pd(II)}} + 0.101$ ). The LLOQ of the proposed optical method for Pd(II) was obtained to be 0.05  $\mu\text{g ml}^{-1}$ , while the LOD and LOQ were calculated to be 0.005 and 0.014  $\mu\text{g ml}^{-1}$ , respectively.

The performance of the suggested optical method was investigated for the determination of Cr(III) using spectroscopic and colorimetric techniques. The digital images of the different concentrations of Cr(III) (0.08 to 0.8  $\mu\text{g ml}^{-1}$ ) were taken at different incubation times [0, 30, and 60 min]. Fig. 7 appears to indicate that after mixing various concentrations of Cr(III) with prob, the color of the solution changes from Persian orange (RGB (204, 147, 92)) to Aloe green (RGB (114, 113, 77)) after a few seconds when the concentration decreases. The colorimetry results indicated that the impact of Cr(III) on the probe color depends on both concentration and reaction time (60 min for Cr(III)). Fig. 7b demonstrates that adding varying concentrations of Cr(III) alters the absorbance intensity of T-AgNPrs colloid, with the absorption spectrum increasing as the concentration of Cr(III) increases. The changes in Cr(III) concentration exhibited a linear relationship to absorbance ratio within the range 0.01–0.8  $\mu\text{g ml}^{-1}$ , represented by the regression equation  $\text{Abs} (A_{\text{sample}}/A_{\text{blank}}) = 1.2015C_{\text{Cr(III)}} + 0.0352$ ,  $R^2 = 0.9906$ . The LLOQ

was determined to be 0.01  $\mu\text{g ml}^{-1}$ , as well as LOD and LOQ for Cr(III) were calculated to be 0.003 and 0.008  $\mu\text{g ml}^{-1}$ , respectively. Furthermore, the relationship between the wavelength of the [T-AgNPrs-DES/Cr(III)] complex ( $\lambda_{\text{max}} = 302 \text{ nm}$ ) and the  $\text{Cr}^{3+}$  concentration ranges from 0.01 to 0.8  $\mu\text{g ml}^{-1}$  is plotted. The wavelength is linearly related to the logarithmic concentration of Cr(III) in this range ( $R^2 = 0.9147$ , regression equation of  $\lambda = -6.9982C_{\text{Cr(III)}} + 303.36$ ). The results show that Cr(III) and T-AgNPrs interact effectively in the DES medium and the proposed optical sensor can be used to perform quantitative analysis of Cr(III).

The validity of the proposed method is examined for Cs(I) in various concentrations. When various concentrations of Cs(I) (0.08 to 0.8  $\mu\text{g ml}^{-1}$ ) were added to T-AgNPrs-DES, the solution color immediately changed from buff (RGB (230, 208, 125)) to Greige (RGB (154, 154, 139)) as the concentration is decreased (as illustrated in Fig. 8a). The Colorimetric results indicate that the Cs(I) effect on the probe color remains constant after 30 minutes of incubation. Two distinct properties are observed when Cs(I) concentration is added: the absorption spectrum of the [T-AgNPrs-DES/Cs(I)] complex at  $\lambda_{\text{max}} = 400$  ( $A_{400}$ ) and the positions of  $\lambda_{\text{max}}$ . The  $A_{400}$  of the  $\lambda_{\text{max}}$  increases with Cs(I) concentrations, as well as  $\lambda_{\text{max}}$  moves to red shift (longer wavelengths); a plot of both changes against the concentrations of Cs(I) is illustrated in Fig. 8c and d. A linear relationship between the absorbance ratio and Cs(I) concentrations (0.08 to 0.8  $\mu\text{g ml}^{-1}$ ) can be observed from Fig. 8c, so that the

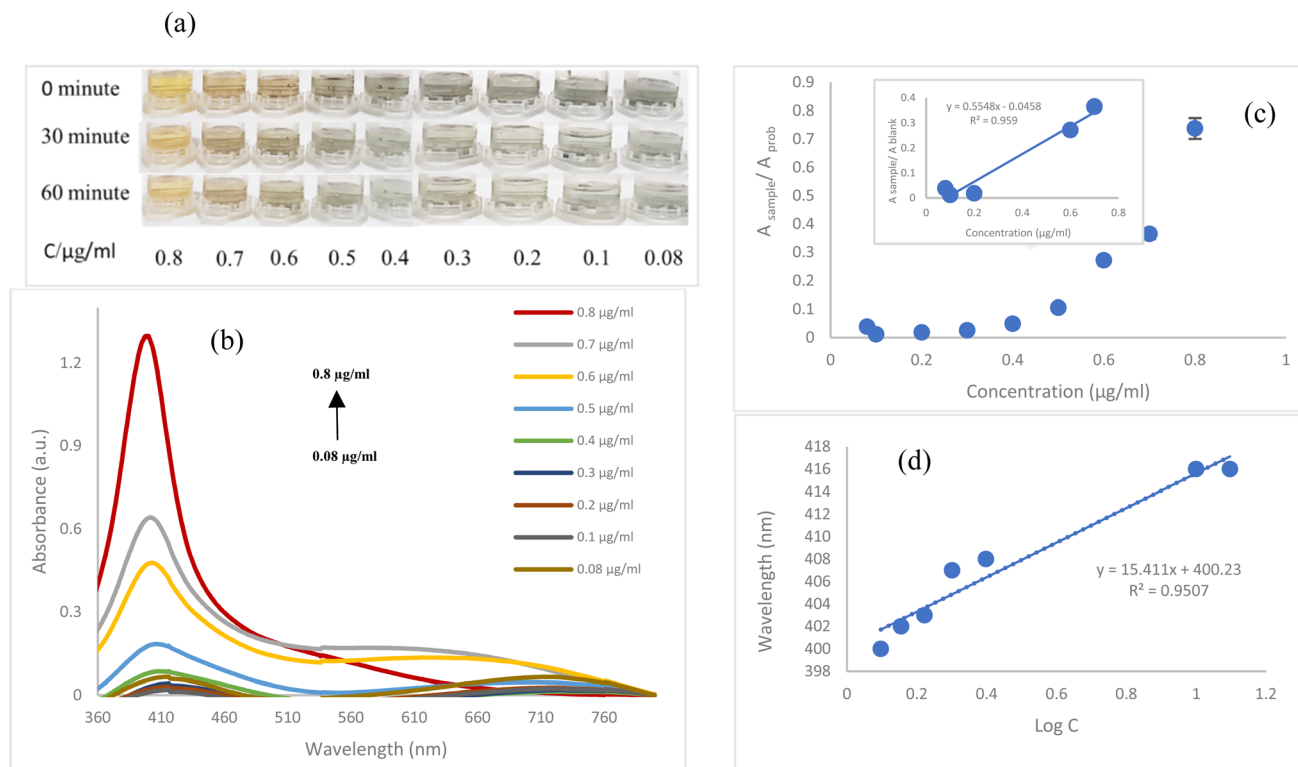


**Fig. 8** Photographic images of T-AgNPs-DES Cs(I) of different concentrations at various incubation times (0, 30, and 60 min) with volume ratio 1 : 1 (a). Absorption spectrum peak of T-AgNPs at different concentrations of Cs(I) in the presence of DES (1 : 1 v/v ratio) after 60 min (b). The calibration curve of absorption ratios ( $A_{\text{sample}}/A_{\text{prob}}$ ) versus Cs(I) concentrations (c) and the wavelength dependence on Cs(I) concentrations (d) from 0.08 to 0.8  $\mu\text{g ml}^{-1}$ .

absorbance at  $\lambda_{\text{max}}$  (400 nm) has increased systematically with the increasing concentration of Cs(I). The regression equation is  $\text{Abs} (A_{\text{sample}}/A_{\text{blank}}) = 0.5548 (\text{Cs(I)}) - 0.0458$  ( $R^2 = 0.952$ ). The LOD and LOQ are calculated to be 0.006 and 0.018  $\mu\text{g ml}^{-1}$ , with LLOQ at 0.08  $\mu\text{g ml}^{-1}$ , respectively. Moreover, the regression equation for this range of logarithmic concentration and  $\lambda_{\text{max}}$  is  $\lambda = 15.834C_{\text{(Cs(I))}} + 399.67$ , with  $R^2 = 0.9724$ . As seen in Fig. 8b. These results suggest that our sensing system can be applied to analyze and detect Cs(I) in various fields.

The reproducibility of the suggested optical system was also investigated. Three concentrations of ions ( $\text{W(IV)}$ ,  $\text{Pd(II)}$ ,  $\text{Cr(III)}$ , and  $\text{Cs(I)}$ ) were measured in triplicate, and RSD was computed for each concentration (Table 2). The total RSD for the mentioned ions was calculated to be 0.13, 0.89, 0.38, and 8.06,

respectively. The results of the reproducibility analysis suggest that this sensor is sufficiently precise to detect candidate ions and demonstrates excellent sensitivity and repeatability.

Important analytical metrics to validate the proposed T-AgNPs-DES are given in Table 2 for all analytes examined. These results indicate that the performance of this newly developed optical sensor is commendable for selected metal ions, as evidenced by its low LOD and LOQ, as well as its high reproducibility. The proposed sensor offers advantages in terms of its rapid response time and straightforward procedures involved. One of the primary features of the proposed colorimetry sensor is that the color of the solution remains stable for a long time due to the presence of DES in the solution. This stability is attributed to the distinctive properties of DES,

**Table 2** Analytical metrics for the proposed method

Analytical parameters	W(vi)	Pd(ii)	Cr(iii)	Cs(i)
Linear range ( $\mu\text{g ml}^{-1}$ )	0.05–0.8	0.05–0.8	0.08–0.8	0.08–0.8
$R^2$	0.8263	0.9947	0.9916	0.952
LOD ( $\mu\text{g ml}^{-1}$ )	0.02	0.005	0.003	0.006
LOQ ( $\mu\text{g ml}^{-1}$ )	0.07	0.014	0.008	0.018
LLOQ ( $\mu\text{g ml}^{-1}$ )	0.05	0.05	0.01	0.08
Repeatability (CV %; 0.1 $\mu\text{g ml}^{-1}$ )	0.04	0.92	0.21	23.65
Repeatability (CV %; 0.4 $\mu\text{g ml}^{-1}$ )	0.15	0.96	0.34	0.27
Repeatability (CV %; 0.8 $\mu\text{g ml}^{-1}$ )	0.2	0.78	0.6	0.26



including low vapor pressure at ambient temperature and high viscosity within the optical system.

### 3.6. Real sample analysis

Biomonitoring is a widely recognized and valid approach to evaluating human exposure to hazardous contaminants, such as heavy metals, in both the workplace and the general population. In this context, urine serves as an excellent biological matrix due to the relatively simple and non-invasive procedure for its collection. Consequently, the analysis of chemical components or metabolites in urine is highly recommended in biological monitoring studies. Thus, measuring the concentration of heavy metals in urine is considered to be the most reliable test for individuals exposed to these substances.<sup>79,80</sup> Therefore, in this study, human urine samples were chosen as the detection matrices to verify the suitability of the proposed optical sensor for determining the investigated analytes. Urine samples were collected from drug-free healthy volunteers. Aqueous standard solutions of candidate ions were added into 2.0 ml of urine samples and centrifuged at 4000 rpm for 10 min. The supernatant was transferred to a 2 ml vial for CE-CL

analysis. The spike method was utilized in this study to determine the concentrations of the analytes under investigation in human urine samples. The calibration curves for different concentrations of the studied ions were plotted to reduce the matrix effect. For this purpose, different ion concentrations were prepared and added to human urine samples. Then, the prepared mixtures were combined with the detection optical probe in a volume ratio of 1 : 1, and their interaction was evaluated using colorimetric and spectrophotometric approaches. The colorimetric assay of T-AgNPrs-DES as a sensing probe was employed for identifying various ions in human urine samples using mobile phone camera at three distinct time intervals (0, 30, and 60 minutes), as illustrated in Fig. 9. The observed absorption spectrum along with the calibration curves resulted from different concentrations in adsorption ratios, are presented in Fig. S14–S17. Based on the colorimetric analyses, the color change that resulted from the combination of ions and T-AgNPrs-DES in the real sample was primarily influenced by concentration rather than reaction time. The analytical parameters obtained from every analysis performed on the human urine sample are listed in Table 3.

0 minutes

30 minutes

60 minutes



Fig. 9 Colorimetric assay of T-AgNPrs-DES as a sensing probe to identify different ions in human urine samples by the Spike method at three distinct incubation reaction times (0, 30, and 60 minutes).

Table 3 Analytical parameters of W(vi), Pd(ii), Cr(iii), and Cs(i) based on the proposed sensing probe of human urine samples

Analytical parameters	W(vi)	Pd(ii)	Cr(iii)	Cr(iii)	Cs(i)
Linear range ( $\mu\text{g ml}^{-1}$ )	0.2–0.8	0.08–0.8	0.5–0.8	0.05–0.4	0.01–0.8
$R^2$	0.9804	0.9956	0.9984	0.9647	0.9935
LOD ( $\mu\text{g ml}^{-1}$ )	0.04	0.002	—	0.01	0.001
LOQ ( $\mu\text{g ml}^{-1}$ )	0.11	0.006	—	0.03	0.003
LLOQ ( $\mu\text{g ml}^{-1}$ )	0.2	0.08	—	0.01	0.01
% RSD (CV %; $0.2 \mu\text{g ml}^{-1}$ , $(n = 3)$ )	0.5	0.1	0.3	—	5.6
% RSD (CV %; $0.5 \mu\text{g ml}^{-1}$ , $(n = 3)$ )	3.4	0.1	1.5	—	5.6
% RSD (CV %; $0.8 \mu\text{g ml}^{-1}$ , $(n = 3)$ )	7.1	0.4	2.8	—	0.1



For all analytes investigated, linearity was evaluated using standard solutions of 0.01, 0.05, 0.08, 0.1, 0.2, 0.3, 0.4, 0.5, 0.6, 0.7, and 0.8  $\mu\text{g ml}^{-1}$ . A linear interval was achieved with a coefficient of determination ( $R^2$ ) for  $\text{W(vi)}$ ,  $\text{Pd(II)}$ ,  $\text{Cr(III)}$ , and  $\text{Cs(I)}$  of 0.9804, 0.9956, 0.9815, and 0.9935, respectively. According to the results described in Table 3, LLOQ values were calculated for  $\text{W(vi)}$ ,  $\text{Pd(II)}$ ,  $\text{Cr(III)}$ , and  $\text{Cs(I)}$  were determined to be 0.2, 0.08, 0.01, and 0.01  $\mu\text{g ml}^{-1}$ , respectively, with lower LOD and LOQ values. The repeatability of the proposed sensor method was assessed by three trials of each analyte at concentrations of 0.2, 0.4, and 0.8  $\mu\text{g ml}^{-1}$ . The RSD values were less than 3.67% (ranging from 0.21% to 3.67%) for all tested cations that confirming repeatability and reproducibility of the method. In summary, the experiments conducted verified that this plasmonic probe exhibits good linearity, relatively high sensitivity, and adequate precision for detecting  $\text{W(vi)}$ ,  $\text{Pd(II)}$ ,  $\text{Cr(III)}$ , and  $\text{Cs(I)}$  in human urine samples. These findings indicate that the T-AgNPrs-based DES system as a sensing prob is notably simpler and less time-consuming for detection and can effectively identify candidate ions in real samples.

### 3.7. Smartphone-based spectrometer

Spectrophotometric instruments are a powerful tool in scientific research and industrial applications because of their adaptability and accuracy. It is extensively used in many different fields, such as environmental monitoring,<sup>79</sup> food evaluation,<sup>80</sup> and pharmaceutical analysis,<sup>81</sup> among numerous other applications. Optical spectroscopy offers significant benefits due to its rapid and non-destructive nature, making it an effective method for qualitative and quantitative analysis. However, despite the simple design, most spectrometers utilized in industrial or laboratory settings are expensive and large and require light-emitting diodes-based to capture the data. Recent progress in electronics and fabrication techniques has made it possible to create portable spectrometers. These spectrometers are commercially available, but they cannot function independently and generally require an external computer for data processing, data collection, and analysis. This requirement significantly increases operational expenses and restricts the scope of potential applications. Due to this limitation resulted has led to the use of common devices like smartphones as spectrometers. Despite some progress in portable smartphone spectroscopy, several improvements are necessary to improve the quality and repeatability of data.<sup>82</sup>

In recent years, spectroscopy techniques using smartphones have gained prominence over bulky traditional equipment because of their numerous advantages, including quick analysis, cost-effectiveness, straightforward manufacturing, portability, and user-friendliness. As a result, their analytical performance is very similar to that of commercial techniques.<sup>83,84</sup> The RGB color (red (R), green (G), and blue (B)) model is the most widely used one, and the measurement of RGB values by various software programs is the basis for the analysis of various types of samples using smartphones.<sup>85</sup> This experiment allows us to analyze Beer's Law using a smartphone by spectrometer measurement principles.<sup>86</sup> Simplicity was an

objective in the development of the protocol, as quick and easy data collection is followed by significantly more efficient data analysis.

**3.7.1 Background theory and experimental setup.** UV/vis spectroscopy is used to investigate how a sample reacts to light. When light passes through the solution, of it may be absorbed and a certain amount of light may be transmitted. The absorbance ( $A$ ) at a specific wavelength is the negative logarithm of the light intensity passing through the sample ( $I$ ) to the light intensity entering the sample ( $I_0$ ) (eqn (1)).

$$A = -\log(I/I_0) \quad (1)$$

In absorption analysis, the Beer–Lambert law is the most crucial principle. According to this law, if the length of the path is not changed, the concentration and absorbance of an ideal solution have a linear relationship.

The color wheel is frequently used for determining the color of light absorbed in solution by a specific chemical species (as illustrated in Fig. S18, upper (see SI)). The correct light source to study the absorption of light must be selected, one that is complementary to the color of the sample under investigation (complementary colors). For this study, the names and codes of the complementary colors of the sample solution were identified on the Colorxs website. The light source, detector, and sample holder are all parts of the experimental apparatus, and they are all oriented orthogonally in the same direction. The computer and smartphone are both outfitted with the proper apps, which act as the color detector and light source, respectively, and are orthogonally aligned in the same direction. Additionally, 1.5 ml vials were used instead of cuvettes.

The PhotoMetrix application (version 1.1.7) (<https://www.photometrix.com.br>) was developed to provide a free tool that can be used for chemical analysis with various analytes and samples and to allow both univariate and multivariate analyses within a single application. This powerful application allows to display of RGB values for a selected area directly on the screen of a smartphone without any additional processing or conversion of digital images. Software includes a setting that allows users to adjust the size of the focused area of color where RGB data is extracted. For this study, the PhotoMetrix PRO software (version 1.1.7) (<https://www.photometrix.com.br>) on the smartphone was used to record RGB data and function as a light. Digital images taken by smartphone cameras were decomposed and processed on the same device using this application, enabling *in situ* analysis. The light source, the computer's LED display, was adjusted to an opposite color sample solution using the RGB app.

To prevent interference from ambient light, blank samples were acquired for each sample. A microtube filled with the blank was placed inside the sample box, and the RGB values of light flowing through a microtube containing the blank were measured on a scale of 0 to 255.

RGB values were also recorded for the solutions with known concentration. The formula  $A = -\log(I/I_0)$  was used to calculate the absorption of individual samples. In this equation, the values of RGB in each sample are represented by  $I$ , while the





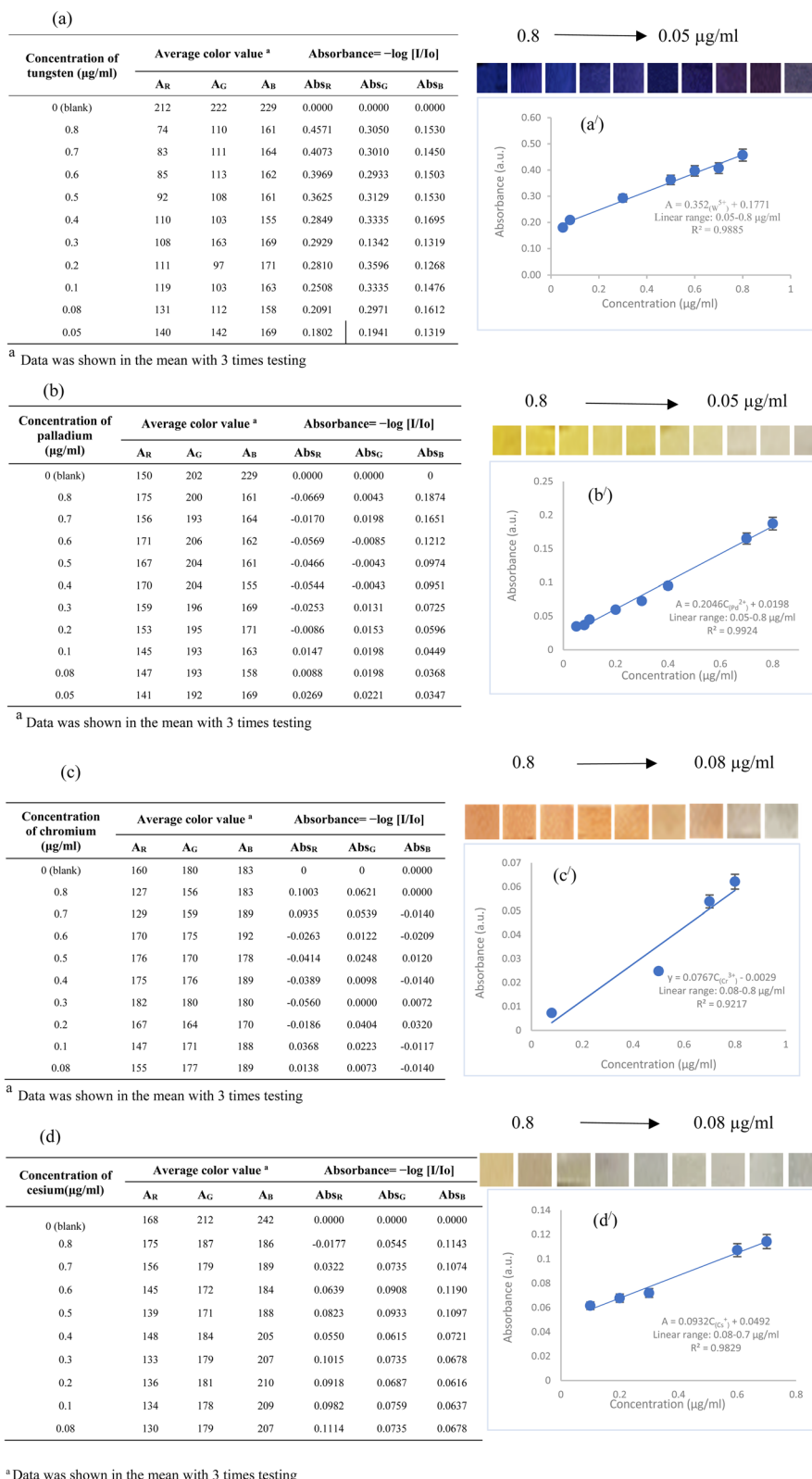


Fig. 10 Average RGB color value and absorbance of (a) tungsten, (b) palladium, (c) chromium, (d) cesium. Calibration curve by absorbance using RGB values from a smartphone-based spectrometer and their photographs (inset) of the different ionic concentrations: (a') tungsten; (b') palladium; (c') chromium; (d') cesium.



values of RGB in the blank solution are indicated by  $I_0$ . As a result, the smartphone-based spectrophotometer that was developed became a portable tool for determining potential analytes on-site.

**3.7.2 The application of the spectrophotometer-based smartphone with the RGB method.** The homemade sample box was designed to allow light to pass through the sample during the absorption measurement. The experimental set-up is detailed in Fig. S19, lower (see SI). In order to view the sample through the mobile screen, the computer screen with the complementary colors of our solution was then positioned behind the sample box as the light source, since the highest absorbance of the colored solution is exhibited in the opposite color. For every solution measurement, the distance between the smartphone's position and the sample box must be constant because a different distance will result in less accuracy of the RGB obtained. Here, we utilized the smartphone-based spectrometer to estimate the absorbance of the colored solution.

The samples of the ion standard solution of the selected ions were prepared in the DES and mixed in the 1 : 1 volume ratio with the probe. Change in the color solution indicated that the reaction was complete. Simple spectroscopy was used to estimate the variation in color intensity of various ion concentrations based on the RGB values (Fig. 10a–d).

A calibration curve was plotted by using the absorbance of the optical sensor, derived from RGB values, against varying concentrations of analytes (Fig. 10a'–d'). The color intensity measurements were recorded using a smartphone (Samsung A54) for the red (R), green (G), and blue (B) for both ion and blank samples. The absorbance values for the samples were calculated by  $A = -\log[I/I_0]$  as described;<sup>87,88</sup>  $I$  = RGB values of the [T-AgNPrs-DES] + ion sample, and  $I_0$  = RGB values of and blank solution. For the constructed smartphone approach, the value between R, G, and B was chosen to form the calibration plot, which resulted in the graph with the highest linearity. The calibration samples were analyzed in triplicate. The smartphone spectrometer's excellent linear response is revealed by the linear regression analysis, in which R, G, B, and B values increase in direct proportion to the concentrations of W(vi), Pd(ii), Cr(iii), and Cs(i), respectively. The resulting coefficients are 0.9885, 0.9924, 0.9217, and 0.9829, respectively. These results suggest that the smartphone-based spectrometer is suitable for quantitative measurement of concentrations.

**3.7.3 Assessing the smartphone-based spectrometer.** Quantitative assessment of performance is an important factor in the development of new proposals. As a result, the findings from the methodology developed for this research were compared with those from a reference method.

The main objective of comparing methods is to identify whether two methods can be used interchangeably based on their compatibility. Linear regression plays a crucial role in assessing the relationship between two measurement methods. This statistical approach aims to find the best linear correlation between data points. The parameters of the calibration curves, LLOQ, and RSD using the reference method and developed method are outlined in Table 4.

The first indicator of the method's performance is the coefficient of correlation ( $R^2$ ). The  $R^2$  values exceeding 0.9 for the four ions selected indicate that the method is satisfactory; but a higher coefficient indicates that the method is more successful. In addition, the LLOQ evaluation term indicates the sensitivity of the method and should be addressed during the development of the method. As shown, the LLOQ values for all analytes are very similar in both methods.

The dynamic linear ranges for W(vi), Pd(ii), Cr(iii), and Cs(i) were comparable; however, the smartphone-based spectrophotometer showed a standard deviation higher than that presented by the commercial spectrophotometer, and no significant differences between the two methods of quantification were identified. This difference is mainly due to the higher noise levels inherent in manual measurements and visual detection with the basic smartphone spectrometer.

It is crucial to highlight those three key factors that significantly impact the results: lighting, the distance between the object and the lens, and CMOS sensors. The issue of lighting can be improved by using a flash, while the distance can be managed by using a support such as a tripod or a selfie stick. Furthermore, selecting a higher-quality camera will provide more accurate estimations of values. The smartphone-based spectrometer employs the same analytical process as the commercial model, and thus the use of a smartphone-based device does not represent a significant reduction in the analysis time for each measurement. But the smartphone-based spectrometer has a lot of benefits, like being inexpensive, portable, and relatively simple to use, which makes it a suitable choice for screening.

**Table 4** Analytical values of merit for determination of W(vi), Pd(ii), Cr(iii), and Cs(i) by smartphone-based and commercial spectrophotometers

Analyte	Linear range of the calibration curve ( $\mu\text{g ml}^{-1}$ )		Sensitivity <sup>b</sup> (LLOQ, $\mu\text{g ml}^{-1}$ )		RSD <sup>c</sup> (%)	
	Smartphone-based SP <sup>a</sup>	Commercial SP	Smartphone-based SP	Commercial SP	Smartphone-based SP	Commercial SP
W(vi)	0.05–0.8 ( $R^2 = 0.9885$ )	0.05–0.8 ( $R^2 = 0.8263$ )	0.05	0.05	3.9	0.13
Pd(ii)	0.05–0.8 ( $R^2 = 0.9924$ )	0.05–0.8 ( $R^2 = 0.99947$ )	0.05	0.05	2.6	0.89
Cr(iii)	0.08–0.8 ( $R^2 = 0.9217$ )	0.01–0.8 ( $R^2 = 0.9906$ )	0.08	0.01	3.2	0.38
Cs(i)	0.08–0.8 ( $R^2 = 0.932$ )	0.08–0.8 ( $R^2 = 0.952$ )	0.08	0.08	10.9	8.09

<sup>a</sup> SP, spectrophotometer. <sup>b</sup> Lowest limitation of quantification (LLOQ). <sup>c</sup> RSD, relative standard deviation, for three replicate measurements of 0.1, 0.4, and 0.8  $\mu\text{g ml}^{-1}$  for all analytes.



The coefficient correlation between absorbance smartphone-based and commercial spectrophotometers for W(vi), Pd(ii), Cr(iii), and Cs(i) was 0.9736, 0.971, 0.9603, and 0.9813, respectively (see Fig. 11). There is a strong correlation between the commercial and smartphone-based devices for selective ions. Overall, this technology represents a major step forward in developing a new generation of portable spectrometry capable of *in situ* measurements.

**3.7.4 Application of the smartphone-based spectrometer in real samples.** To further demonstrate the performance of the smartphone-based spectrometer in a real application, selected ions were measured in human urine samples. Standard ion solution was prepared in DES to a concentration ranging from 0.01 to 0.8  $\mu\text{g ml}^{-1}$ . Initially, the prepared urine sample with a standard ion solution was mixed in a microcentrifuge tube (at a 1 : 1 v/v ratio). Then, the prepared mixtures were added to the optical probe solution in a volume ratio of 1 : 1, and their absorbance was measured by the developed smartphone-based spectrometer.

The RGB values of different ion concentrations in human urine samples were estimated by simple spectroscopy (Fig. S19a–d (see SI)). A calibration curve was plotted by absorbance obtained from the RGB values, against the different concentrations of the analyte (Fig. S19a'–d'). The linear correlation coefficient was 0.9959 and 0.9855 for  $\text{Pd}^{2+}$  and  $\text{Cs}^+$  (linear ranges: 0.01–0.8  $\mu\text{g ml}^{-1}$ ), respectively. Due to the different color spectra observed in human urine samples of tungsten and chromium, two specific concentration ranges were defined for the calibration curves to be constructed. The tungsten

concentration ranges were 0.4–0.8 and 0.01–0.3  $\mu\text{g ml}^{-1}$ , respectively, while the chromium concentration ranges were 0.05–0.4 and 0.4–0.8  $\mu\text{g ml}^{-1}$ , with coefficients of 0.9995 and 0.9247, respectively.

Fig. 12 displays the coefficient correlation for selected ions, obtained from both the standard method and the smartphone-based spectrometer in real samples. The results indicate a strong correlation between the measurements of absorbance from commercial and smartphone-based spectrometers. The suggested smartphone spectrometer presents a novel method for accurately measuring ion concentrations. This approach could serve as an alternative for bulky instrumentation in a laboratory. We designed an innovative, handheld, and portable smartphone-based spectrophotometer that doesn't require any external light source, lens, or filter. This straightforward spectrometer makes use of a computer as the light source, a smartphone as the detector, and the Photometrix app. LLOQ achieved for W(vi), Pd(ii), Cr(iii), and Cs(i) were 0.05, 0.05, 0.08, and 0.08, respectively. It is successfully used for the quantitation of the absorption of the mentioned ions in human urine samples in this study. This lightweight spectrometer can be fabricated in minutes and used with excellent accuracy. This device produced readouts with high spectral accuracy that were comparable to or superior to those of a commercial spectrometer. This promising analytical tool's portability and ease of use allow it to be used in a variety of applications by everyone. Furthermore, when this portable device is coupled with a smartphone, it can be considered a substitute detection system for commercial UV-vis spectrometers.

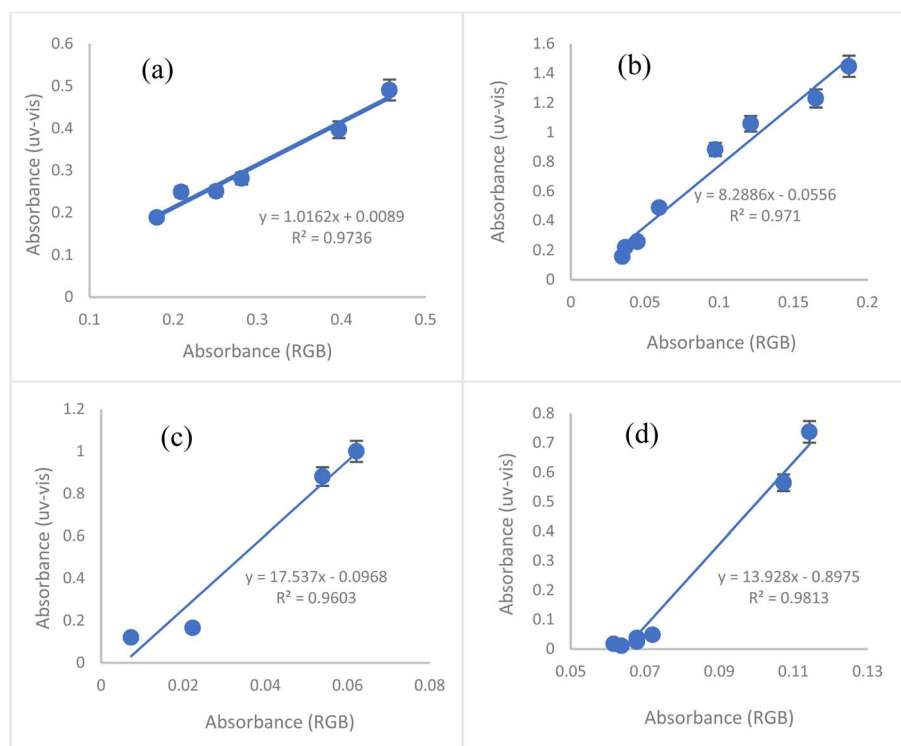


Fig. 11 Calibration curve overlay between smartphone-based and commercial spectrophotometers of standard solutions of (a) tungsten, (b) palladium, (c) chromium, and (d) cesium.



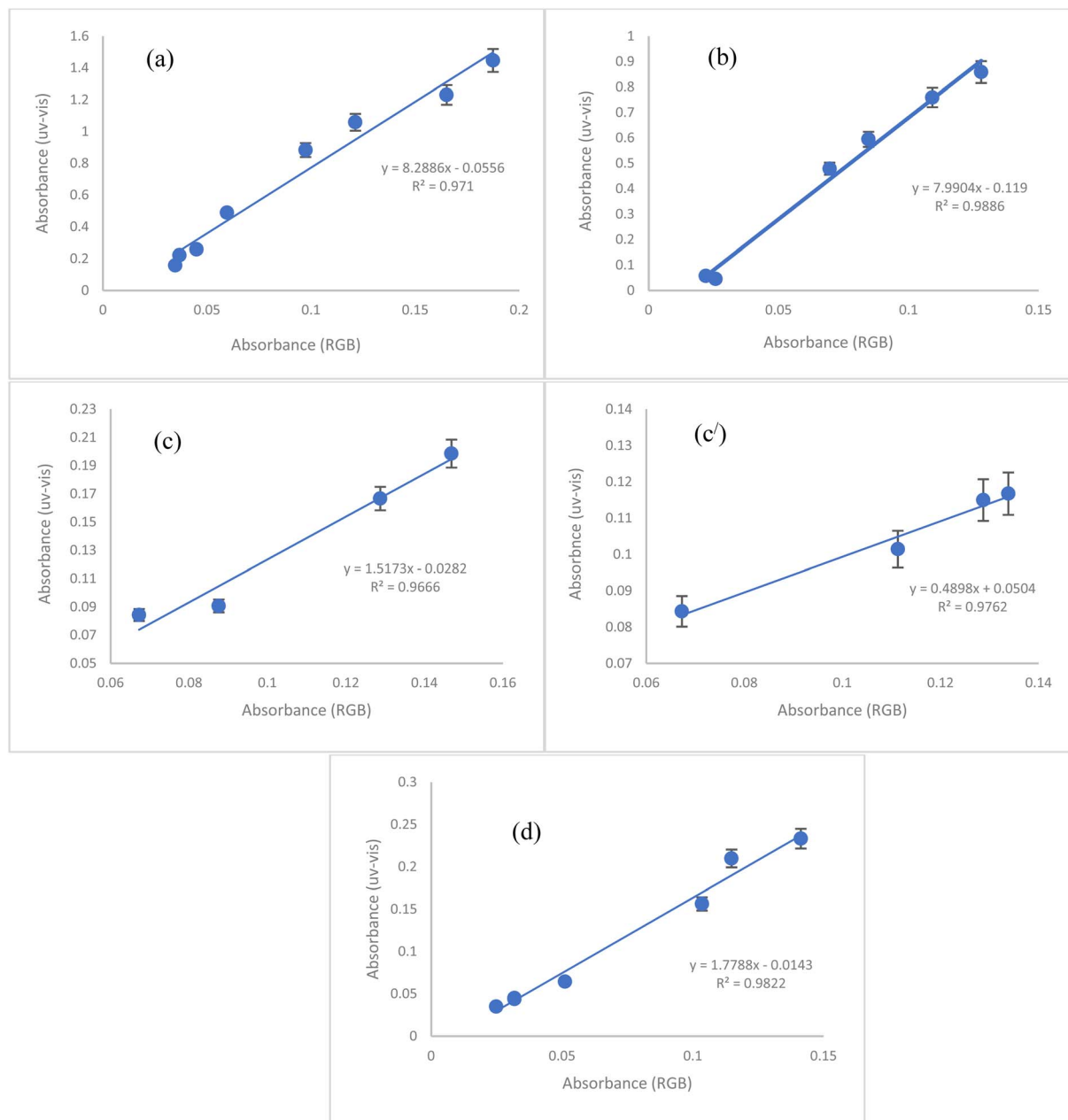


Fig. 12 Calibration curve overlay between standard method and smartphone method of human urine samples: (a) tungsten, (b) palladium, (c) (0.4 to 0.8  $\mu\text{g ml}^{-1}$ ) and c' (0.05 to 0.4  $\mu\text{g ml}^{-1}$ ) chromium, (d) cesium.

The combination of nanoparticle-based materials with DESs is a relatively new approach that allows researchers to exploit synergies between the two components and thus increase sensor performance. The advanced optical and electronic properties of noble metal nanoparticles, combined with the chemical versatility of DESs, result in sensors that are highly sensitive and selective for the detection of target analytes. This research is the first comprehensive study to date on the combined use of these two materials in the development of optical sensors. In addition, we provide an outlook for possible future developments in this promising area.

## 4. Conclusion

We have developed a straightforward and easily manufacturable approach for preparing T-AgNPs-DES as an optical probe. Additionally, it is a strong candidate for green chemistry applications in the field due to its environmentally friendly nature. This optical sensor has been utilized to detect four cations ( $\text{W(VI)}$ ,  $\text{Pd(II)}$ ,  $\text{Cr(III)}$ , and  $\text{Cs(I)}$ ) with high sensitivity and appropriate selectivity. The complexation of ions with T-AgNPs in a DES medium forms the basis for detection. Notably, research has shown that T-AgNPs exhibits different spectral behavior in the DES medium. The results of the study are





significant as they suggest that a strong hydrogen bond between T-AgNPrs and ChCl-EG (DES) drives the self-assembly and detection mechanisms. To our knowledge, this is the first instance of metal ion analysis utilizing the association of T-AgNPrs-based DES. The proposed optical sensor demonstrates high sensitivity for detecting candidate ions with a low LOD (0.02, 0.005, 0.003, and 0.006  $\mu\text{g ml}^{-1}$  for W(VI), Pd(II), Cr(III), and Cs(I), respectively) across a linear range of 0.01–0.8  $\mu\text{g ml}^{-1}$ . The advantages of this method include: (I) a simple, cost-effective, and user-friendly colorimetric probe, (II) rapid and sensitive detection, and (III) shorter analysis times. The developed plasmonic probe procedure shows high potential for determining metal ions in human urine samples, based on analytical figures of merit. Consequently, all results indicate that this sensing system possesses satisfactory sensitivity and can be applied to determine candidate ions across various fields.

## Conflicts of interest

There are no conflicts to declare.

## Data availability

Access to the data used in this study is available upon request and may be subject to approval by the data provider. Restrictions may apply to the availability of these data, which were used under license for this study. Interested parties are encouraged to contact the corresponding author for further information on accessing the data. All relevant data supporting the findings of this study are available within the article and its SI files, or from the corresponding author upon reasonable request. Access to some data may be restricted due to privacy or ethical restrictions. Any restrictions to data availability will be disclosed at the time of data request.

Supplementary information is available. See DOI: <https://doi.org/10.1039/d5ra04031k>.

## Acknowledgements

The results of this study were obtained from the PhD dissertation (3400808) registered at the Esfahan University of Medical Sciences. We are grateful to Tabriz University of Medical Sciences, particularly the Pharmaceutical Analysis Research Center (Tabriz, Iran), for their instrumental assistance and resources provided during this study.

## References

- 1 M. F. Romero-Zarazua, J. L. Sanchez-Salas, M. A. Quiroz-Alfaro, E. R. Bandala and M. A. Méndez-Rojas, Occupational exposure to heavy metals in a metal-mechanical auto part manufacturing plant in Puebla, Mexico, *Int. J. Environ. Health Eng.*, 2015, **4**(1), 8.
- 2 E. Berhan, Management commitment and its impact on occupational health and safety improvement: a case of iron, steel and metal manufacturing industries, *Int. J. Workplace Health Manag.*, 2020, **13**(4), 427–444.
- 3 A. M. Donoghue, Occupational health hazards in mining: an overview, *Occup. Med.*, 2004, **54**(5), 283–289.
- 4 M. Li, H. Gou, I. Al-Ogaidi, and N. Wu, *Nanostructured Sensors for Detection of Heavy Metals: a Review*, ACS Publications, 2013.
- 5 S. Martin, and W. Griswold, Human health effects of heavy metals. *Environmental Science and Technology briefs for citizens*, 2009, 15(5)pp. 1–6.
- 6 M. Junaid, M. Z. Hashmi, R. N. Malik and D.-S. Pei, Toxicity and oxidative stress induced by chromium in workers exposed from different occupational settings around the globe: A review, *Environ. Sci. Pollut. Res.*, 2016, **23**, 20151–20167.
- 7 K. Rehman, F. Fatima, I. Waheed and M. S. H. Akash, Prevalence of exposure of heavy metals and their impact on health consequences, *J. Cell. Biochem.*, 2018, **119**(1), 157–184.
- 8 Z. Fu and S. Xi, The effects of heavy metals on human metabolism, *Toxicol. Mech. Methods*, 2020, **30**(3), 167–176.
- 9 B. O. Anyanwu, A. N. Ezejiofor, Z. N. Igweze and O. E. Orisakwe, Heavy metal mixture exposure and effects in developing nations: an update, *Toxics*, 2018, **6**(4), 65.
- 10 F. O. Ohiagu, P. Chikezie, C. Ahaneku and C. Chikezie, Human exposure to heavy metals: toxicity mechanisms and health implications, *Mater. Sci. Eng.*, 2022, **6**(2), 78–87.
- 11 S. F. Sulthana, U. M. Iqbal, S. B. Suseela, R. Anbazhagan, R. Chinthaginjala, D. Chitathuru, *et al.*, Electrochemical sensors for heavy metal ion detection in aqueous medium: a systematic review, *ACS Omega*, 2024, **9**(24), 25493–25512.
- 12 A. N. Berlina, A. V. Zherdev and B. B. Dzantiev, Progress in rapid optical assays for heavy metal ions based on the use of nanoparticles and receptor molecules, *Microchim. Acta*, 2019, **186**, 1–39.
- 13 H. N. Kumar, D. Nagaraju, Z. Yhobu, P. Shivakumar, K. M. Kumara, S. Budagumpi, *et al.*, Recent advances in on-site monitoring of heavy metal ions in the environment, *Microchem. J.*, 2022, **182**, 107894.
- 14 A. Amirjani and D. F. Haghshenas, Ag nanostructures as the surface plasmon resonance (SPR)-based sensors: a mechanistic study with an emphasis on heavy metallic ions detection, *Sens. Actuators, B*, 2018, **273**, 1768–1779.
- 15 A. Helaluddin, R. S. Khalid, M. Alaama and S. A. Abbas, Main analytical techniques used for elemental analysis in various matrices, *Trop. J. Pharm. Res.*, 2016, **15**(2), 427–434.
- 16 M. Jin, H. Yuan, B. Liu, J. Peng, L. Xu and D. Yang, Review of the distribution and detection methods of heavy metals in the environment, *Anal. Methods*, 2020, **12**(48), 5747–5766.
- 17 S. Sikdar and M. Kundu, A review on detection and abatement of heavy metals, *ChemBioEng Rev.*, 2018, **5**(1), 18–29.
- 18 X. Zhou, J. Nie and B. Du, Functionalized ionic microgel sensor array for colorimetric detection and discrimination of metal ions, *ACS Appl. Mater. Interfaces*, 2017, **9**(24), 20913–20921.
- 19 M. Zare-Moghadam, M. Shamsipur, F. Molaabasi and B. Hajipour-Verdom, Chromium speciation by isophthalic acid-doped polymer dots as sensitive and selective fluorescent probes, *Talanta*, 2020, **209**, 120521.



- 20 A. Saadati, F. Farshchi, M. Hasanzadeh, Y. Liu and F. Seidi, Colorimetric and naked-eye detection of arsenic (iii) using a paper-based microfluidic device decorated with silver nanoparticles, *RSC Adv.*, 2022, **12**(34), 21836–21850.
- 21 R. Abdel-Karim, Y. Reda and A. Abdel-Fattah, Nanostructured materials-based nanosensors, *J. Electrochem. Soc.*, 2020, **167**(3), 037554.
- 22 D. Nunes, A. Pimentel, A. Gonçalves, S. Pereira, R. Branquinho, P. Barquinha, *et al.*, Metal oxide nanostructures for sensor applications, *Semicond. Sci. Technol.*, 2019, **34**(4), 043001.
- 23 V. Srikanth, M. Shastri, M. Sindhu Sree, M. Navya Rani, P. D. Shivaramu, and D. Rangappa, Nanostructure Material-Based Sensors for Environmental Applications, *Nanostructured Materials for Environmental Applications*, 2021, pp. 565–589.
- 24 M. J. McGrath, C. N. Scanail, M. J. McGrath, and C. N. Scanail, Sensing and sensor fundamentals, *Sensor Technologies: Healthcare, Wellness, and Environmental Applications*, 201315–50.
- 25 A. Munawar, Y. Ong, R. Schirhagl, M. A. Tahir, W. S. Khan and S. Z. Bajwa, Nanosensors for diagnosis with optical, electric and mechanical transducers, *RSC Adv.*, 2019, **9**(12), 6793–6803.
- 26 J. H. Heo, M. Sung, T. Q. Trung, Y. Lee, D. H. Jung, H. Kim, *et al.*, Sensor design strategy for environmental and biological monitoring, *EcoMat*, 2023, **5**(5), e12332.
- 27 M. Li, S. K. Cushing and N. Wu, Plasmon-enhanced optical sensors: a review, *Analyst*, 2015, **140**(2), 386–406.
- 28 Y. Li, Q. Liao, W. Hou and L. Qin, Silver-based surface plasmon sensors: fabrication and applications, *Int. J. Mol. Sci.*, 2023, **24**(4), 4142.
- 29 S. Kim, J. M. Kim, J. E. Park and J. M. Nam, Nonnoble-metal-based plasmonic nanomaterials: recent advances and future perspectives, *Adv. Mater.*, 2018, **30**(42), 1704528.
- 30 N. T. T. Phuong, V. Q. Dang, T. N. Bach, B. X. Khuyen, H. K. T. Ta, H. Ju, *et al.*, Functionalized silver nanoparticles for SERS amplification with enhanced reproducibility and for ultrasensitive optical fiber sensing in environmental and biochemical assays, *RSC Adv.*, 2022, **12**(48), 31352–31362.
- 31 S. Agrawal, M. Bhatt, S. K. Rai, A. Bhatt, P. Dangwal and P. K. Agrawal, Silver nanoparticles and its potential applications: A review, *J. Pharmacogn. Phytochem.*, 2018, **7**(2), 930–937.
- 32 B. Tang, S. Xu, X. Hou, J. Li, L. Sun, W. Xu, *et al.*, Shape evolution of silver nanoplates through heating and photoinduction, *ACS Appl. Mater. Interfaces*, 2013, **5**(3), 646–653.
- 33 Z.-F. Pu, B.-C. Wu, Y.-H. Tan, Q.-L. Wen, J. Ling and Q.-E. Cao, Selective aggregation of silver nanoprisms induced by monohydrogen phosphate and its application for colorimetric detection of chromium (III) ions, *J. Anal. Test.*, 2021, **5**(3), 225–234.
- 34 M. A. Raza, Z. Kanwal, A. Rauf, A. N. Sabri, S. Riaz and S. Naseem, Size-and shape-dependent antibacterial studies of silver nanoparticles synthesized by wet chemical routes, *Nanomaterials*, 2016, **6**(4), 74.
- 35 J. Jana, M. Ganguly and T. Pal, Enlightening surface plasmon resonance effect of metal nanoparticles for practical spectroscopic application, *RSC Adv.*, 2016, **6**(89), 86174–86211.
- 36 K. Khurana and N. Jaggi, Localized surface plasmonic properties of Au and Ag nanoparticles for sensors: a review, *Plasmonics*, 2021, **16**(4), 981–999.
- 37 A. Philip and A. R. Kumar, The performance enhancement of surface plasmon resonance optical sensors using nanomaterials: A review, *Coord. Chem. Rev.*, 2022, **458**, 214424.
- 38 L. Wang, M. Hasanzadeh Kafshgari and M. Meunier, Optical properties and applications of plasmonic-metal nanoparticles, *Adv. Funct. Mater.*, 2020, **30**(51), 2005400.
- 39 Y. N. Wijaya, J. Kim, W. M. Choi, S. H. Park and M. H. Kim, A systematic study of triangular silver nanoplates: one-pot green synthesis, chemical stability, and sensing application, *Nanoscale*, 2017, **9**(32), 11705–11712.
- 40 Z. Chen, C. Zhang, Q. Wu, K. Li and L. Tan, Application of triangular silver nanoplates for colorimetric detection of H<sub>2</sub>O<sub>2</sub>, *Sens. Actuators, B*, 2015, **220**, 314–317.
- 41 A. Yakoh, P. Rattanarat, W. Siangproh and O. Chailapakul, Simple and selective paper-based colorimetric sensor for determination of chloride ion in environmental samples using label-free silver nanoprisms, *Talanta*, 2018, **178**, 134–140.
- 42 E. Detsri, P. Seeharaj and C. Sriwong, A sensitive and selective colorimetric sensor for reduced glutathione detection based on silver triangular nanoplates conjugated with gallic acid, *Colloids Surf., A*, 2018, **541**, 36–42.
- 43 E. Detsri, Novel colorimetric sensor for mercury (II) based on layer-by-layer assembly of unmodified silver triangular nanoplates, *Chin. Chem. Lett.*, 2016, **27**(10), 1635–1640.
- 44 A. A. Furletov, V. V. Apyari, A. V. Garshev, P. A. Volkov and S. G. Dmitrienko, Silver triangular nanoplates as a colorimetric probe for sensing thiols: Characterization in the interaction with structurally related thiols of different functionality, *Microchem. J.*, 2019, **147**, 979–984.
- 45 C. Grazioli, G. Faura, N. Dossi, R. Toniolo, F. Tubaro, F. Terzi, *et al.*, A colorimetric paper-based smart label soaked with a deep-eutectic solvent for the detection of malondialdehyde, *Sens. Actuators, B*, 2021, **329**, 129174.
- 46 M. Laosuwan, C. Poonsawat, R. Burakham, S. Srijaranai and S. Mukdasai, A novel liquid colorimetric probe for highly selective and sensitive detection of lead (II), *Food Chem.*, 2021, **363**, 130254.
- 47 M. Laosuwan, N. Gissawong, N. Butwong, S. Srijaranai and S. Mukdasai, Facile liquid colorimetric sensor using high-density deep eutectic solvent for trace detection and speciation of iron in milk, *Spectrochim. Acta, Part A*, 2022, **272**, 121020.
- 48 M. Atilhan and S. Aparicio, Molecular dynamics simulations of metal nanoparticles in deep eutectic solvents, *J. Phys. Chem. C*, 2018, **122**(31), 18029–18039.



- 49 Z. Yuan, H. Liu, W. F. Yong, Q. She and J. Esteban, Status and advances of deep eutectic solvents for metal separation and recovery, *Green Chem.*, 2022, **24**(5), 1895–1929.
- 50 T. El Achkar, H. Greige-Gerges and S. Fourmentin, Basics and properties of deep eutectic solvents: a review, *Environ. Chem. Lett.*, 2021, **19**, 3397–3408.
- 51 K. A. Omar and R. Sadeghi, Database of deep eutectic solvents and their physical properties: A review, *J. Mol. Liq.*, 2023, **384**, 121899.
- 52 E. L. Smith, A. P. Abbott and K. S. Ryder, Deep eutectic solvents (DESS) and their applications, *Chem. Rev.*, 2014, **114**(21), 11060–11082.
- 53 Q. Zhang, K. D. O. Vigier, S. Royer and F. Jérôme, Deep eutectic solvents: syntheses, properties and applications, *Chem. Soc. Rev.*, 2012, **41**(21), 7108–7146.
- 54 W. Chen, Z. Xue, J. Wang, J. Jiang, X. Zhao and T. Mu, Investigation on the thermal stability of deep eutectic solvents, *Acta Phys.-Chim. Sin.*, 2018, **34**(8), 904–911.
- 55 Y. Chen, D. Yu, Z. Liu, Z. Xue and T. Mu, Thermal, chemical, electrochemical, radiolytic and biological stability of ionic liquids and deep eutectic solvents, *New J. Chem.*, 2022, **46**(37), 17640–17668.
- 56 S. Khandelwal, Y. K. Tailor and M. Kumar, Deep eutectic solvents (DESS) as eco-friendly and sustainable solvent/catalyst systems in organic transformations, *J. Mol. Liq.*, 2016, **215**, 345–386.
- 57 Z. Shojaeifard and B. Hemmateenejad, Deep and dip: immobilization on paper substrate using deep eutectic solvent to fabricate reusable dip immersion colorimetric sensor arrays, *Sens. Actuators, B*, 2022, **356**, 131379.
- 58 L. Li, Y. Liu, Z. Wang, L. Yang and H. Liu, Development and applications of deep eutectic solvent derived functional materials in chromatographic separation, *J. Sep. Sci.*, 2021, **44**(6), 1098–1121.
- 59 Y. Kiliç, B. T. Zaman, S. Bakirdere and N. Özdoğan, Dual techniques for trace copper determination: DES/Dithizone based liquid phase microextraction-flame atomic absorption spectrophotometry and digital image based colorimetric probe, *Food Chem.*, 2024, **432**, 137244.
- 60 M. S. Mondal, A. Paul and M. Rhaman, Recycling of silver nanoparticles from electronic waste via green synthesis and application of AgNPs-chitosan based nanocomposite on textile material, *Sci. Rep.*, 2023, **13**(1), 13798.
- 61 M. S. Hsu, Y. W. Cao, H. W. Wang, Y. S. Pan, B. H. Lee and C. L. Huang, Time-Dependent surface plasmon resonance spectroscopy of silver nanoprisms in the presence of halide ions, *ChemPhysChem*, 2010, **11**(8), 1742–1748.
- 62 H. Xu, Y. Kong, J. Peng, X. Song, Y. Liu, Z. Su, *et al.*, Comprehensive analysis of important parameters of choline chloride-based deep eutectic solvent pretreatment of lignocellulosic biomass, *Bioresour. Technol.*, 2021, **319**, 124209.
- 63 *Choline-based Deep Eutectic Solvent for Extractive Oxidative Desulfurization of Model Oil. E3S Web of Conferences*, ed. T. Ravi, A. N. Masri, and I. M. Ibrahim, EDP Sciences, 2024.
- 64 I. Alfurayj, R. Pandian, S. Springer and C. Burda, Choline Fluoride-Ethylene glycol deep eutectic solvent mixture–Synthesis and physicochemical properties, *J. Mol. Liq.*, 2023, **386**, 122454.
- 65 L. Feng, H. Meng, Y. Lu and C. Li, Efficient and reversible absorption of HCl gas by ChCl-based deep eutectic solvents-Insights into the absorption behavior and mechanism, *Sep. Purif. Technol.*, 2022, **281**, 119994.
- 66 J. E. Millstone, S. J. Hurst, G. S. Métraux, J. I. Cutler and C. A. Mirkin, Colloidal gold and silver triangular nanoprisms, *Small*, 2009, **5**(6), 646–664.
- 67 C. N. Lunardi, A. J. Gomes, F. S. Rocha, J. De Tommaso and G. S. Patience, Experimental methods in chemical engineering: Zeta potential, *Can. J. Chem. Eng.*, 2021, **99**(3), 627–639.
- 68 S.-J. Yoon, Y.-S. Nam, H.-J. Lee, Y. Lee and K.-B. Lee, Colorimetric probe for Ni<sup>2+</sup> based on shape transformation of triangular silver nanoprisms upon H<sub>2</sub>O<sub>2</sub> etching, *Sens. Actuators, B*, 2019, **300**, 127045.
- 69 M. I. Martín, I. García-Díaz and F. López, Properties and perspective of using deep eutectic solvents for hydrometallurgy metal recovery, *Miner. Eng.*, 2023, **203**, 108306.
- 70 R. K. Ibrahim, M. Hayyan, M. A. AlSaadi, S. Ibrahim, A. Hayyan and M. A. Hashim, Physical properties of ethylene glycol-based deep eutectic solvents, *J. Mol. Liq.*, 2019, **276**, 794–800.
- 71 H. Hinterwirth, S. K. Wiedmer, M. Moilanen, A. Lehner, G. Allmaier, T. Waitz, *et al.*, Comparative method evaluation for size and size-distribution analysis of gold nanoparticles, *J. Sep. Sci.*, 2013, **36**(17), 2952–2961.
- 72 J. Chen, Y. Wang, X. Wei, Z. Liu, F. Xu, H. Li, *et al.*, A novel “turn-off” fluorescence assay based on acid-copper nanoclusters in deep eutectic solvent micelles for co-aggregation inducing fluorescence enhancement and its application, *Talanta*, 2021, **223**, 121731.
- 73 L. Nicoli, S. Sodomaco, P. Lafiosca, T. Giovannini and C. Cappelli, Atomistic Multiscale Modeling of Colloidal Plasmonic Nanoparticles, *ACS Phys. Chem. Au*, 2024, **4**(6), 669–678.
- 74 H. Sharma, N. Kaur, A. Singh, A. Kuwar and N. Singh, Optical chemosensors for water sample analysis, *J. Mater. Chem. C*, 2016, **4**(23), 5154–5194.
- 75 K. Ngamchuea, C. Batchelor-McAuley, S. V. Sokolov and R. G. Compton, Dynamics of silver nanoparticles in aqueous solution in the presence of metal ions, *Anal. Chem.*, 2017, **89**(19), 10208–10215.
- 76 S. Tamilselvan, R. Soniya, R. Vasantharaja, M. Kannan, S. Supriya, B. P. D. Batvari, *et al.*, Silver nanoparticles based spectroscopic sensing of eight metal ions in aqueous solutions, *Environ. Res.*, 2022, **212**, 113585.
- 77 V. S. Sousa and M. R. Teixeira, Aggregation kinetics and surface charge of CuO nanoparticles: the influence of pH, ionic strength and humic acids, *Environ. Chem.*, 2013, **10**(4), 313–322.
- 78 M. Kosmulski and E. Mączka, Zeta potential and particle size in dispersions of alumina in 50–50 w/w ethylene glycol-water mixture, *Colloids Surf., A*, 2022, **654**, 130168.



- 79 M. N. Fiddler, I. Begashaw, M. A. Mickens, M. S. Collingwood, Z. Assefa and S. Bililign, Laser spectroscopy for atmospheric and environmental sensing, *Sensors*, 2009, **9**(12), 10447–10512.
- 80 J. T. Alander, V. Bochko, B. Martinkauppi, S. Saranwong and T. Mantere, A review of optical nondestructive visual and near-infrared methods for food quality and safety, *Int. J. Spectrosc.*, 2013, **2013**(1), 341402.
- 81 M. Jamrógiewicz, Application of the near-infrared spectroscopy in the pharmaceutical technology, *J. Pharm. Biomed. Anal.*, 2012, **66**, 1–10.
- 82 A. J. Das, A. Wahi, I. Kothari and R. Raskar, Ultra-portable, wireless smartphone spectrometer for rapid, non-destructive testing of fruit ripeness, *Sci. Rep.*, 2016, **6**(1), 32504.
- 83 M. Sargazi and M. Kaykhaii, Application of a smartphone based spectrophotometer for rapid in-field determination of nitrite and chlorine in environmental water samples, *Spectrochim. Acta, Part A*, 2020, **227**, 117672.
- 84 Y. Xing, Q. Zhu, X. Zhou and P. Qi, A dual-functional smartphone-based sensor for colorimetric and chemiluminescent detection: A case study for fluoride concentration mapping, *Sens. Actuators, B*, 2020, **319**, 128254.
- 85 M. L. Firdaus, H. Apriyoanda, I. Isnain, S. Wyantuti and D. R. Eddy, Quantitative analysis of Cr (III) and Cr (VI) using gold nanoparticles with UV-vis spectrometry and smartphone colorimetric-sensing, *Iran J. Chem. Chem. Eng.*, 2023, **42**(3), 722–730.
- 86 T. S. Kuntzleman and E. C. Jacobson, Teaching Beer's law and absorption spectrophotometry with a smart phone: a substantially simplified protocol, *J. Chem. Educ.*, 2016, **93**(7), 1249–1252.
- 87 B. Keskin, A. Üzer and R. Apak, Colorimetric sensing of ammonium perchlorate using methylene blue-modified gold nanoparticles, *Talanta*, 2020, **206**, 120240.
- 88 Y. Wang, X. Liu, P. Chen, N. T. Tran, J. Zhang, W. S. Chia, *et al.*, Smartphone spectrometer for colorimetric biosensing, *Analyst*, 2016, **141**(11), 3233–3238.

